

1 Seismic wave modeling of fluid-saturated fractured porous rock: 2 Including fluid pressure diffusion effects of discrete distributed large- 3 scale fractures

4 Yingkai Qi^{1,2}, Xuehua Chen^{1,2}, Qingwei Zhao^{1,2}, Xin Luo¹, Chunqiang Feng³

5 ¹State Key Laboratory of Oil & Gas Reservoir Geology and Exploitation, Chengdu University of Technology, Chengdu,
6 610059, China

7 ²Key Laboratory of Earth Exploration & Information Techniques of Ministry of Education, Chengdu University of Technology,
8 Chengdu, 610059, China

9 ³Exploration & Development Research Institute of Henan Oilfield, Sinopec, 473000, China

10 *Correspondence to:* Xuehua Chen (chen_xuehua@163.com)

11 **Abstract.** The scattered seismic waves of fractured porous rock are strongly affected by the wave-induced fluid pressure
12 diffusion effects between the compliant fractures and the stiffer embedding background. To include these poroelastic effects
13 in seismic modeling, we develop a numerical scheme for discrete distributed large-scale fractures embedded in fluid-saturated
14 porous rock. Using Coates and Schoenberg's local effective medium theory and Barbosa's dynamic linear slip model
15 characterized by complex-valued and frequency-dependent fracture compliances, we derive the effective viscoelastic
16 compliances in each spatial discretized cell by superimposing the compliances of the background and the fractures. The
17 effective governing equations for fractured porous rocks are viscoelastic anisotropic and numerically solved by mixed-grid
18 stencil frequency-domain finite-difference method. The main advantage of our proposed modeling scheme over poroelastic
19 modeling schemes is that the fractured domain can be modeled using a viscoelastic solid, while the rest of the domain can be
20 modeled using an elastic solid. We have tested the modeling scheme in a single fracture model, a fractured model, and a
21 modified Marmousi model. The good consistency between the scattered waves off a single horizontal fracture calculated using
22 our proposed scheme and the poroelastic modeling validates that our modeling scheme can properly capture the FPD effects.
23 In the case of a set of aligned fractures, the scattered waves from the top and bottom of the fractured reservoir are strongly
24 influenced by the FPD effects, and the reflected waves from the underlying formation can retain the relevant attenuation and
25 dispersion information. The effective governing equations of the fractured porous rock are then characterized by the derived
26 anisotropic, complex valued, and frequency dependent effective compliances. We numerically solved the effective governing
27 equations by mixed grid stencil frequency domain finite difference method. The good consistency between the scattered
28 waves off a single horizontal fracture calculated using our proposed scheme and those calculated using the poroelastic linear
29 slip model shows that our modeling scheme can properly include the FPD effects. We also find that for a P point source, the
30 amplitudes of the scattered waves from a single horizontal fracture are strongly affected by the fluid stiffening effects due to
31 fluid pressure diffusion, while for an S point source, the scattered waves are less sensitive to fluid pressure diffusion. In the

32 ease of the conjugate fracture system, the scattered waves from the bottom of the fractured reservoir and the reflected waves
33 from the underlying formation are attenuated and dispersed by the FPD effects for both P and S point sources. The proposed
34 numerical modeling scheme can also be used to improve migration quality and the estimation of fracture mechanical
35 characteristics in inversion.

36 1 Introduction

37 Fluid saturated porous rocks in a reservoir, which rock in the reservoir characterized by a heterogeneous internal structure
38 consisting of a solid skeleton and interconnected fluid-filled voids, are often permeated by much more compliant and
39 permeable fractures. Although the fractures typically occupy only a small volume, they tend to dominate the overall mechanical
40 and hydraulic properties of the reservoir (Liu et al., 2000; Gale et al., 2014). Thus, fracture detection, characterization and
41 imaging are of great importance for reservoir prediction and production. Seismic waves are widely used for these purposes
42 because their behaviors (amplitude, phase and anisotropy) are strongly affected by the fractures (Chapman, 2003; Gurevich,
43 2003; Brajanovski et al., 2005; Carcione et al., 2011; Rubino et al., 2014). Therefore, appropriate numerical modeling methods
44 are required for the interpretation, migration and inversion of seismic data from porous media containing discrete distributed
45 fractures.

46 Biot's poroelastic theory (Biot, 1956a; b) is the fundamental theory to describe elastic wave propagation in fluid porous media,
47 including the dynamic interactions between rock and pore fluid. However, the original theory, assuming a macroscopically
48 homogeneous porous media saturated by a single fluid phase, is fail to explain the measured velocity dispersion and attenuation
49 of seismic waves (Nakagawa et al., 2007). In recent decades, many researchers have found that if porous media contains
50 mesoscale heterogeneity, a local fluid-pressure gradient will be induced at a scale comparable to the fluid pressure diffusion
51 length at the seismic frequency band, thus causing significant velocity dispersion and attenuationIn recent decades, many
52 researchers found that if porous media contains mesoscale heterogeneity (ignored by Biot), a local fluid pressure gradient will
53 be induced by the passing wave at scale comparable to the wave induced fluid pressure diffusion length (the wavelength of
54 slow P wave), causing significant velocity dispersion and velocity attenuation at seismic frequency band (White et al., 1975;
55 Dutta and Odé, 1979; Johnson, 2001; and Müller et al. 2008; Norris, 1993; Gurevich et al., 1997; Gelinsky and Shapiro, 1997;
56 Kudarova et al., 2016). Fractures embedded in homogeneous porous background are special heterogeneities, exhibiting strong
57 mechanical contrasts with background. When seismic waves travel through fluid saturated fractured porous rocks, local fluid
58 pressure gradients will be induced between the fractures and the background in response to the strong compressibility contrast.
59 To return the equilibrium state, fluid pressure diffusion (FPD) occurs between the fractures and the embedding background,
60 which in turn changes the fluid stiffening effect on the fractures and thus their mechanical compliances depending on frequency
61 (Barbosa et al., 2016a, b).

When fractures with spacing and length apertures and lengths much smaller than the wavelengths are uniformly and regularly distributed, unified distributed in porous rock, the properties of the fractured rock are homogeneous at macroscopic scale and can be described by a representative elementary volume (REV). Various effective medium theories are available for estimating the fracture-induced anisotropy, attenuation and dispersion in a poroelastic context behaviors (Hudson, 1981; Thomsen, 1995; Chapman, 2003; Brajanovski et al., 2005; Krzikalla et al. 2011; Galvin et al., 2015; Guo et al., 2017a; b). However, large-scale fractures with much larger spacing and length typically have a more complex discrete distribution rather than a regular one, therefore the properties of rocks containing such fractures cannot be modeled by the effective medium theory. In contrast, the linear slip model (LSM) (Schoenberg, 1980), which represents individual fractures as nonwelded interfaces with discontinuous displacement tensors, is not limited by the assumption of regular distribution and can be used to model the discretely distributed fractures. Due to the discrete distribution, the effects of large-scale fractures are not uniform and vary spatially, which mean that their effects cannot be represented by a single REV. In the framework of LSM, two numerical schemes are available to assess the seismic response of discrete distributed large-scale fractures, the local effective-medium schemes (Coates and Schoenberg, 1995; Igel et al., 1997; Vlastos et al., 2003; Oelke, et al., 2013) and the explicit interface scheme (Zhang, 2005; Cui et al., 2018; Khokhlov, et al., 2021). The local effective-medium scheme uses a very coarse mesh to discretize background media and incorporates the additional effects of fractures within each discretized cell based on LSM, that is, it regards each discretized cell as a REV. The advantage is that it requires no special treatment of the displacement discontinuity conditions on the fractures, which means no additional memory and computation costs. The explicit interface scheme uses a very fine mesh to discretize fractures and directly treats the displacement discontinuity across each fracture without any equivalent treatment, resulting an expensive memory and computation costs. The discrete distributed large scale fractures (the presence of spatial correlations of fractures), however, cannot be modeled by any above mentioned effective medium theories originally for macroscopically uniformly distributed fractures. The seismic response of individual fracture is mostly assessed in the framework of the linear slip model (LSM) by modeling a fracture as a nonwelded interface across which the displacement tensors are assumed to be discontinuous while the stress tensors are continuous (Schoenberg, 1980). Various local numerical schemes have been developed for discrete distributed large scale fractures. The most widely used scheme is local effective medium schemes (Coates and Schoenberg, 1995; Igel et al., 1997; Vlastos et al., 2003; Oelke, et al., 2013) that determine and incorporate the behavior of fracture induced media within each spatial discretized cell. The advantage of using the local effective medium is that it requires no special treatment of the displacement discontinuity conditions on the fractures. An alternative scheme is the explicit interface scheme that directly treat the displacement discontinuity across each fracture (Zhang, 2005; Cui et al., 2018; Khokhlov, et al., 2021).—

The common aspect of the aforementioned numerical modeling schemes is that they are all implemented in a purely elastic framework-LSM with real-valued compliances boundary and represent both the embedding background and fractures as elastic solids, thus the impact of FPD effects on seismic scattering can't be accounted for. A dynamic linear slip model incorporating

94 FPD effects should be considered when implementing numerical modeling of seismic wave propagating in fluid saturated
95 porous rocks containing discrete distributed large-scale fractures. Rubino et al. (2015) proposed a frequency-dependent
96 complex-valued normal compliance for regularly distributed planar fractures (a set of aligned fractures) with a separation much
97 smaller than the prevailing seismic wavelength. Despite the ability of including the FPD across the fractures, the model is not
98 suitable for modeling discrete distributed fractures. Nakagawa and Schoenberg (2007) developed an extended LSM for a single
99 fracture in the context of poroelasticity. The proposed model representing both the background and the fracture as poroelastic
100 media can appropriately incorporate the frequency related effects, but it will also result in a higher computational consuming
101 and more memory requirements. In the context of viscoelasticity, Barbosa et al. (2016a) developed a viscoelastic linear slip
102 model (VLSM) for an individual fracture with explicit complex-valued and frequency-dependent fracture compliances, to
103 account for the impact of FPD on the fracture stiffness. That provides a viscoelasticity-based modeling algorithm for discrete
104 distributed large-scale fractures with smaller computational costs and memory requirements than the poroelasticity based
105 modeling.

106 In this paper, we develop a viscoelastic numerical modeling scheme to simulate seismic wave propagation in fluid-saturated
107 porous media containing discrete distributed large-scale fractures. To capture the FPD effects between the fractures and
108 background, we use the local effective medium theory based on Barbosa's VLSM to derive the effective anisotropic
109 viscoelastic compliances in each numerical cell by superimposing the compliances of the background and the fractures. The
110 effective anisotropic viscoelastic governing equations of the fractured porous rock are then numerically solved using mixed-
111 grid stencil frequency-domain finite-difference method (FDFD) (Hustedt, et al. 2004; Operto, et al. 2009; Liu et al., 2018).

112 Compare to poroelastic modeling scheme, the main advantage of our modeling scheme is that it uses VLSM-based viscoelastic
113 modeling to account for FDP effects in the domain permeated by fractures, while in the rest fracture-free domain, it uses elastic
114 modeling. To validate the proposed viscoelastic modeling scheme can capture the impact of FPD effects on seismic wave
115 scattering, we compare the scattered waves of a single horizontal fracture obtained using our proposed modeling scheme with
116 ~~those obtained using~~ poroelastic modeling scheme and elastic modeling scheme. Numerical examples of a fractured reservoir
117 are presented to demonstrate that the proposed modeling scheme can properly simulate the wave attenuation and dispersion
118 due to the FPD effects between the fracture system and background. A set of rock physics models were generated by the
119 Marmousi model to test the proposed modeling scheme and code. ~~A complex modified Marmousi model is also use to test the~~
120 ~~proposed modeling scheme and code.~~ The scheme can be used not only to study the impact of mechanical and hydraulic of
121 fracture properties on seismic scattering but can also to improve migration quality and the estimation of fracture mechanical
122 characteristics in inversion.

123 **2 Review of the LSM**

124 **2 The elastic models**

125 The LSM was originally proposed by Schoenberg (1980) to represent a solid- or fluid-infilled fracture permeated in a pure
126 solid background, and then extended by other researchers (e.g. Nakagawa, Barbosa) to represent a poroelastic fracture to
127 include the FPD effects. We briefly review the original LSM and its poroelastic and viscoelastic extensions.

128 **2.1 The original LSM**

129 Schoenberg (1980) presented the original LSM in the context of elasticity, representing both the background and the fracture
130 as elastic solids. The original LSM assumes that across a fracture surface the stresses are continuous while the displacements
131 are discontinuous. The discontinuous displacement vector of a horizontal fracture is linearly related to the stress tensor through
132 the fracture compliance, which can be written as:

$$\begin{aligned} [u_x] &= Z_T \sigma_{xz}, \\ [u_y] &= Z_T \sigma_{yz}, \\ [u_z] &= Z_N \sigma_{zz}, \end{aligned} \quad (1)$$

133 where $[u_i]$ are the discontinuous displacement components, σ_{ij} are the stress components, $Z_N = h/H$ and $Z_T = h/\mu$ are the
134 normal and tangential compliance of the fracture, respectively. H and μ are the P-wave and shear modulus of the fracture,
135 and h is the thickness of the fracture. Due to the simple expression, the original LSM can be easily incorporated into the local
136 effective medium theory to model seismic wave scattering off large-scale fractures. However, the original LSM was derived
137 in a purely elastic context, only suitable for fractures filled with pure solids or fluids, thus it is not competent to describe the
138 FPD effects.

139 The two most widely used non-attenuated and non-dissipative elastic models for fractured porous media are the low- and high-
140 frequency limits elastic LSM that ignore the FPD effects between the background and the fractures. The two elastic models
141 can be used to determine the effective anisotropic elastic moduli of the fractured porous rock.

142 **2.1 The low-frequency limits elastic linear slip models (LFLSM)**

143 The presence of fractures in a homogeneous and isotropic porous rock results in an effective anisotropic medium. The effective
144 compliance matrix of the dry fractured rock \mathbf{S}^{dry} can be obtained using the LSM (Schoenberg and Sayers, 1995):

$$\mathbf{S}^{dry} = \mathbf{S}_b^{dry} + \mathbf{Z}_0, \quad (1)$$

145 where \mathbf{S}_b^{dry} is the isotropic compliance matrix of the dry background medium in the absent of fractures, and \mathbf{Z}_0 is the excess
146 compliance matrix due to the dry fractures. For a single set of rotationally invariant fractures, \mathbf{Z}_0 can be written as
147 (Schoenberg and Sayers, 1995):

$$Z_{ij,0} = \frac{Z_T}{4} (\delta_{ik} n_i n_j + \delta_{jk} n_i n_t + \delta_{ki} n_j n_t + \delta_{kj} n_i n_t) + (Z_{N_d} - Z_T) n_i n_j n_k n_t, \quad (2)$$

where n_i is the component of the local unit normal to the fracture surface, Z_{N_d} and Z_T are the drained normal fracture compliance and tangential fracture compliance, respectively, as functions of fracture thickness h^e and the drained longitudinal modulus H_d^e and shear moduli μ^e of the fracture (Brajanovski et al., 2005):

$$Z_{N_d} = \frac{h^e}{H_d^e}, \quad Z_T = \frac{h^e}{\mu^e}. \quad (3)$$

Since the fluid pressure is uniform in the low frequency limit, the corresponding effective stiffness matrix C_{ij}^{sat} of the fluid saturated rock can be obtained using the anisotropic Gassmann equation (Gurevich, 2003):

$$C_{ij,ff}^{\text{sat}} = C_{ij}^{\text{dry}} + \alpha_i \alpha_j M_{dry}, \quad i, j = 1, \dots, 6. \quad (4)$$

The anisotropic Biot-Willis coefficients α_m are:

$$\alpha_m = 1 - \frac{\sum_{n=1}^3 C_{mn}^{\text{dry}}}{3K_g}, \quad m = 1, 2, 3, \quad (5)$$

$\alpha_4 = \alpha_5 = \alpha_6 = 0$. The Biot's fluid storage modulus M is

$$M_{dry} = \frac{K_f}{(1 - K_0^*/K_g) - \phi(1 - K_g/K_f)}, \quad (6)$$

where K_g denotes the grain solid bulk modulus, K_f the pore fluid bulk modulus, and K_0^* the generalized drained bulk modulus, defined as

$$K_0^* = \frac{1}{9} \sum_{i=1}^3 \sum_{j=1}^3 C_{ij}^{\text{dry}}. \quad (7)$$

2.2 The high-frequency limits elastic linear-slip models (HFLSM)

In the high-frequency limit, the fractures are hydraulically isolated from the saturated background medium. The effective compliance matrix of the saturated background medium permeated by the dry fractures can be expressed as (Guo et al., 2016):

$$S_{hf}^{\frac{1}{2}} = S_B^{\text{sat}} + Z_0, \quad (8)$$

where S_B^{sat} is the isotropic compliance matrix of the saturated background medium in the absent of fractures. The effective stiffness coefficients of the saturated fractured rock can be written as:

$$C_{ij,hf}^{\text{sat}} = C_{ij,ff}^{\frac{1}{2}} + \alpha_i^{\frac{1}{2}} \alpha_j^{\frac{1}{2}} M_+, \quad i, j = 1, \dots, 6, \quad (9)$$

where $\alpha^{\frac{1}{2}}$ and M_+ can be again calculated using Eqs. (5)-(7) but replacing the solid grains bulk modulus K_g with saturated bulk modulus of the background K_m^{sat} , the overall porosity ϕ with the fracture porosity ϕ_e .

2.2 Nakagawa's PLSM

3 Nakagawa's poroelastic LSM (PLSM)

Nakagawa and Schoenberg (2007) presented a PLSM in the framework of poroelasticity, representing the fracture as a highly compliant and porous thin isotropic, homogeneous layer embedded in a much stiffer and much less porous background

(Nakagawa et al., 2007, Barbosa et al., 2016a). Nakagawa and Schoenberg (2007) presented a PLSM in the framework of poroelasticity, representing the fracture as a highly compliant and porous thin layer embedded in a much stiffer and much less porous background (Barbosa et al., 2016a). Similar to the classic LSM, the PLSM assumes that across a fracture surface the stress tensor is continuous while the displacement tensor is discontinuous. The discontinuous displacement components for a horizontal fracture are (Nakagawa and Schoenberg, 2007):

$$\begin{aligned} [u_x] &= Z_T \sigma_{xz}, \\ [u_y] &= Z_T \sigma_{yz}, \\ [u_z] &= Z_{N_D} (\sigma_{zz} + \alpha P_f), \\ [w_z] &= -\alpha Z_{N_D} \left(\sigma_{zz} + \frac{1}{B} P_f \right), \end{aligned} \quad (2)$$

$$[u_x] = Z_T \tau_{xz}, \quad (10a)$$

$$[u_y] = Z_T \tau_{yz}, \quad (10b)$$

$$[u_z] = Z_{N_D} (\tau_{zz} + \alpha P_f), \quad (10c)$$

$$[w_z] = -\alpha Z_{N_D} \left(\tau_{zz} + \frac{1}{B} P_f \right), \quad (10d)$$

where $Z_{N_D} = h/H_D$ and $Z_T = h/\mu$ are the fracture's drained normal compliance and tangential compliance, respectively, H_D

and H_U are the fracture's drained and undrained P -wave modulus, respectively, α is the Biot's effective stress coefficient of

the fracture, $B = \alpha M/H_U$ is the fracture's uniaxial Skempton coefficient. Since the PLSM represents both the background

and the fracture as poroelasticity, it is capable to describe the discontinuous displacement of the relative fluid in addition to

the solid, implying that it can properly handle the FPD effects between the background and the fracture, where the parameter

$B = \alpha M/H_U$, and the definition of drained normal fracture compliance Z_{N_D} and tangential fracture compliance Z_T are the

same as those in LFLEM. Since the PLSM represents both the background and the fracture as poroelasticity, it is capable to

describe the discontinuous displacement of the relative fluid in addition to the solid, implying that it can properly handle the

FPD effects between the background and the fracture. Although it is difficult to incorporate the PLSM into the effective

medium theory to obtain the effective moduli of the fractured porous rock, these boundary conditions can be easily incorporated

into poroelastic finite-difference algorithm for modeling seismic wave scattering off large-scale fractures parallel to the

coordinate axis. An alternative wavenumber domain method for modeling the scattered waves by poroelastic fractures is

presented by Nakagawa and Schoenberg (2007) based on the PLSM.

2.3 Barbosa's VLSM

4 Barbosa's viscoelastic LSM (VLSM)

Barbosa et al. (2016a) derived a VLSM that account for the FPD effects between a fracture and background and the resulting

stiffening effect impact on the fracture. The background is assumed to be not impacted by the FPD and can be represented by an elastic solid, whose properties are computed according to Gassmann's equation. By representing fractures as extremely thin viscoelastic layers, the poroelastic effects were incorporated into the classical LSM through complex-valued and frequency-dependent compliances. These compliances characterize the mechanical properties of the fluid-saturated fracture.

4.1 The boundary conditions of VLSM

The discontinuous displacement components of the VLSM (Barbosa et al., 2016a) for a horizontal fracture are

$$\begin{aligned} [u_x] &= Z_T \sigma_{xz}, \\ [u_y] &= Z_T \sigma_{yz}, \\ [u_z] &= Z_N \sigma_{zz} + Z_X \varepsilon_{xx}, \end{aligned} \quad (3)$$

$$[u_x] = Z_T \tau_{xz}, \quad (11a)$$

$$[u_y] = Z_T \tau_{yz}, \quad (11b)$$

$$[u_z] = Z_N \tau_{zz} + Z_X \varepsilon_{xx}, \quad (11c)$$

where Z_N and Z_T are generalized normal and tangential compliances of the fracture respectively, and Z_X is a dimensionless parameter that related to the coupling between horizontal and vertical deformation of the fracture. The normal compliance Z_N and additional parameter Z_X are complex-valued and frequency-dependent, while the tangential compliance $Z_T = h/\mu$ is the same as for elastic and poroelastic models. [The two frequency-dependent and complex-valued compliances are:](#)

$$\begin{aligned} Z_N &= Z_{N_U} + Z_{N_D} \frac{G_1(1+i)}{\sqrt{\omega} + G_2(1+i)}, \\ Z_X &= -\frac{G_3(1+i)}{\sqrt{\omega} + G_4(1+i)}, \end{aligned} \quad (4)$$

[The three effective fracture parameters are given by Barbosa et al. \(2016a\)](#)

$$\eta_N = \frac{\eta_{N_D} [\alpha \eta_{N_U} D_{p_x}^b - 2B \gamma_{p_x}^b i k_{p_x}^b - 2\alpha i k_{p_x}^b (1/\gamma_{p_x}^b + 2B)]}{\alpha \eta_{N_D} D_{p_x}^b - 2B \gamma_{p_x}^b i k_{p_x}^b}, \quad (12a)$$

$$\eta_X = \frac{-4k_{p_x}^b \alpha^b \eta_T M^b \mu^b (\alpha H_U^b M - \alpha^b H_U M^b)}{(H_U^b)^2 (h H_U \omega \eta_f^b + 2k_{p_x}^b M H_D k^b)}. \quad (12b)$$

We rewrite Eqs. (12a) (12b) as

$$Z_N = Z_{N_D} + Z_{N_D} \frac{G_2(1+i)}{\sqrt{\omega} + G_2(1+i)}, \quad (13a)$$

$$Z_X = \frac{G_3(1+i)}{\sqrt{\omega} + G_4(1+i)}, \quad (13b)$$

where $Z_{N_U} = h/H_U$ and $Z_{N_D} = h/H_D$ are the fracture's undrained and drained normal compliance respectively, ω is the angular frequency. The four real-valued parameters G_1 , G_2 , G_3 and G_4 are defined as

$$G_1 = \frac{\kappa^b}{\eta Z_{N_D}} \frac{(B^b - B^f)^2}{\sqrt{D^b}}, \quad G_2 = \frac{\kappa^b}{\eta Z_{N_D}} \frac{B^f}{\alpha^f \sqrt{D^b}}, \quad G_3 = \frac{2\sqrt{2}\alpha^b \mu^b (B^f - B^b) \sqrt{D^b}}{H_D^b}, \quad G_4 = \frac{\sqrt{2}\kappa^b D^f}{Z_T \mu^f \kappa^f \sqrt{D^b}}, \quad (5)$$

228 where κ is the permeability, η is the viscosity of the fluid, $D = \frac{\kappa H_D M}{\eta H_U}$ is the diffusivity, the other parameters are defined in

229 the same way as in poroelasticity. The parameters in equation (5) with superscripts b correspond to background properties and
230 the parameters with superscripts c correspond to fracture parameters.

231 In the low-frequency limit, the two frequency-dependent and complex-valued parameters become:

232

$$Z_N = Z_{N_U} + Z_{N_D} \frac{G_1}{G_2}, \quad (6)$$

$$Z_X = -\frac{G_3}{G_4}.$$

233 The frequency-independent and real-valued parameters in equation (6) indicate the elastic behavior of the fracture, which is
234 expected, since the fluid pressure between the fracture and background at low frequencies has enough time to equilibrate within
235 a half-wave period (i.e. the fracture is softest), resulting in no dispersion and attenuation of the seismic waves.

236 In the high-frequency limit, the two frequency-dependent and complex-valued parameters become:

237

$$Z_N = Z_{N_U}, \quad (7)$$

$$Z_X = 0.$$

238 Equation (7) indicates that the fracture model collapses to an elastic thin layer model in the high-frequency limit, which is
239 consistent with the original LSM that computes the properties of both fracture and background using Gassmann's equations.
240 This because at high frequencies, the fluid pressure between the fracture and background has no time to equilibrate within a
241 half-wave period, i.e. the fracture is hardest and behaves as being sealed. The VLSM considering FPD effects can be
242 incorporated into the local effective medium theory to simulate the poroelastic seismic response of large-scale fractures, while
243 its low- and high-frequency limits can be used to model the elastic seismic response.

244 In the VLSM, according to Barbosa et al. (2016a), there are two distinct frequency regimes frequency-dependent fracture
245 compliance due to FPD, and the characteristic frequency for the transition between the two regimes is:

246

$$\omega_m = 2\pi f_m = \left(\frac{2}{h} \right)^2 \left(\frac{e_b^2}{e_f^2 + e_f e_b} \right) D_f, \quad (8)$$

247 where h is the thickness of the fracture, D is the diffusivity, $e = \kappa/\eta\sqrt{D}$, the superscripts b and f correspond to background
248 fracture parameters, respectively.

249

$$G_1 = \frac{\sqrt{\kappa b} (B^b - B^e)^2}{\eta N^b \eta N_D}, \quad G_2 \approx \sqrt{\frac{\kappa b}{\eta N^b \eta N_D}}, \quad (14a)$$

250

$$G_3 = \frac{2\sqrt{2} \alpha^b \mu^b (B^b - B^e) \sqrt{D^b}}{H_D^b}, \quad G_4 = \frac{\sqrt{2} \kappa^b D^e}{h^e \kappa^e \sqrt{D^b}}, \quad (14b)$$

251 where the parameters with superscripts b correspond to background properties and the parameters with superscripts e
252 correspond to fracture parameters. In Eqs. (14a) (14b), D is the diffusivity defined as $D = \kappa N/\eta$ ($N = H_D M/H_U$), and the

253 dimensionless parameter B defined as $B = \alpha M / H_d$. H_d , H_d and μ are the corresponding undrained P -wave modulus,
 254 drained P -wave modulus and shear modulus. The Barbosa's VLSM can properly capture the FPD effects between a fracture
 255 and background.

256 3 Seismic modeling of fractured porous rock

257 In this section, we focus on the implementation of seismic modeling of fluid-saturated porous media containing discrete
 258 distributed large-scale fractures in 2D case. We develop a viscoelastic modeling scheme based on the VLSM and local effective
 259 medium theory (Coates and Schoenberg, 1995) to incorporate the FPD effects between fractures and background. To validate
 260 that the proposed viscoelastic modeling scheme can capture the impact of FPD effects on seismic wave scattering of fractures,
 261 we outline the implementation of poroelastic modeling scheme using an explicit application of the PLSM.

262 3.1 viscoelastic modeling based on VLSM

263 4.2 The effective viscoelastic-anisotropic stiffness matrix based on Barbosa's VLSM

264 To incorporate the VLSM into viscoelastic finite-difference modeling algorithms, we adopt Coates and Schoenberg's local
 265 effective media theory (1995) to account for the property of each fracture. We first provide the specific derivation of the
 266 effective viscoelastic-anisotropic stiffness matrix of the numerical cell by superimposing the compliances of the background
 267 and the fractures. we give the specific derivation of the effective viscoelastic-anisotropic stiffness matrix of the numerical grids
 268 on a fracture based on Coates and Schoenberg's local effective medium theory (1995). The porous background is assumed to
 269 be unaffected by the FPD in the presence of fractures because of the small amount of diffusing fluid and large compliance
 270 contrast between background and fluid. Thus, the rock background can be represented by an elastic homogeneous solid and its
 271 strain tensor ϵ^b can be expressed as

$$272 \epsilon_{ij}^b = s_{ijkl}^b \sigma_{kl}, \quad (i, j = x, y, z) \quad (9)$$

$$273 \epsilon_{ij}^b = s_{ijkl}^b \sigma_{kl}, \quad (15)$$

274 where the compliance tensor s^b is computed according to Gassmann's equation (Rubino et al., 2015), and σ is the average stress
 275 tensor. The exceed strain tensor ϵ^c induced by a single fracture with surface S in a representative volume V (e.g. the volume of
 276 numerical cell) is given by (Hudson and Knopoff, 1989; Sayers and Kachanov, 1995; Liu, et al., 2000)

$$277 \epsilon_{ij}^c = s_{ijkl}^c \sigma_{kl} = \frac{1}{2V} \int ([u_i] n_j + [u_j] n_i) dS, \quad (10)$$

$$278 \epsilon_{ij}^c = s_{ijkl}^c \sigma_{kl} = \frac{1}{2V} \int ([u_i] n_j + [u_j] n_i) dS, \quad (16)$$

279 where s^c is the extra compliance tensor resulting from the fractures, $[u_i]$ is the i th component of the displacement
 280 discontinuity on S , n_i is the i th component of the fracture normal. Note that equation (10) Eq. (16) is applicable to finite,

281 nonplanar fractures in the long wavelength limit, i.e., the applied stress is assumed to be constant over the representative
282 volume.

283 If we assume that the interface of the fracture is normal to the z -axis (fracture normal vector \mathbf{n} is $(0,0,1)$), substituting [equation \(3\)](#) into [equation \(10\)](#), [Eqs. \(11a\)–\(11c\)](#) into [Eq. \(16\)](#), we can obtain the nonzero element of the exceed fracture strain tensor

$$\begin{aligned}\varepsilon_{xz}^c &= \frac{S}{V} Z_T \sigma_{xz}, \\ \varepsilon_{yz}^c &= \frac{S}{V} Z_T \sigma_{yz}, \\ \varepsilon_{zz}^c &= \frac{S}{V} (Z_N \sigma_{zz} + Z_X \varepsilon_{xx}^b).\end{aligned}\quad (11)$$

286 $\varepsilon_{xx}^e = \frac{S}{V} Z_T \tau_{xz}, \quad (17a)$

287 $\varepsilon_{yz}^e = \frac{S}{V} Z_T \tau_{yz}, \quad (17b)$

288 $\varepsilon_{zz}^e = \frac{S}{V} (Z_N \tau_{zz} + Z_X \varepsilon_{xx}^b), \quad (17c)$

289 For simplicity, we use an abbreviated Voigt notation for the stresses, strains, and stiffness and compliance tensors, and rewrite
290 the equation (9) and (11) as:

291 Then the exceed fracture strain tensor ε_{ij}^e and the background strain tensor ε_{ij}^b can be written in matrix form in Voigt notation
292 $\hat{\varepsilon}^b = \hat{\mathbf{S}}^b \hat{\boldsymbol{\sigma}}, \quad (12)$

293 $\hat{\varepsilon}^c = \frac{S}{V} (\hat{\mathbf{Z}}^I \hat{\boldsymbol{\sigma}} + \hat{\mathbf{Z}}^{II} \hat{\varepsilon}) = \frac{S}{V} (\hat{\mathbf{Z}}^I + \hat{\mathbf{Z}}^{II} \hat{\mathbf{S}}^b) \hat{\boldsymbol{\sigma}}, \quad (13)$

294 where $\hat{\varepsilon} = [\varepsilon_{xx}, \varepsilon_{yy}, \varepsilon_{zz}, 2\varepsilon_{yz}, 2\varepsilon_{xz}, 2\varepsilon_{xy}]^T$ is the strain matrix, $\hat{\boldsymbol{\sigma}} = [\sigma_{xx}, \sigma_{yy}, \sigma_{zz}, \sigma_{yz}, \sigma_{xz}, \sigma_{xy}]^T$ is the stress matrix, and $\hat{\mathbf{S}}^b$ is the
295 compliance matrix of background. Note that in this paper the " \wedge " symbol is used to indicate matrices to distinguish them
296 from tensors, which is used to distinguish a tensor. The 6×6 fracture compliance matrix $\hat{\mathbf{Z}}^I$ and additional dimensionless
297 matrix $\hat{\mathbf{Z}}^{II}$ according to the Voigt notation are defined as

$$\hat{\mathbf{Z}}^I = \begin{bmatrix} 0 & 0 & 0 & 0 & 0 & 0 \\ 0 & 0 & 0 & 0 & 0 & 0 \\ 0 & 0 & Z_N & 0 & 0 & 0 \\ 0 & 0 & 0 & Z_T & 0 & 0 \\ 0 & 0 & 0 & 0 & Z_T & 0 \\ 0 & 0 & 0 & 0 & 0 & 0 \end{bmatrix}, \quad \hat{\mathbf{Z}}^{II} = \begin{bmatrix} 0 & 0 & 0 & 0 & 0 & 0 \\ 0 & 0 & 0 & 0 & 0 & 0 \\ Z_X & 0 & 0 & 0 & 0 & 0 \\ 0 & 0 & 0 & 0 & 0 & 0 \\ 0 & 0 & 0 & 0 & 0 & 0 \\ 0 & 0 & 0 & 0 & 0 & 0 \end{bmatrix}, \quad (14)$$

299 $\mathbf{e}^b = \mathbf{S}^b \boldsymbol{\sigma}, \quad (18)$

300 $\mathbf{e}^e = \frac{S}{V} (\mathbf{Z}_T \boldsymbol{\sigma} + \mathbf{Z}_Z \mathbf{e}^b) = \frac{S}{V} (\mathbf{Z}_T + \mathbf{Z}_Z \mathbf{S}^b) \boldsymbol{\sigma}, \quad (19)$

301 where the strain matrix $\mathbf{e} = [\varepsilon_{11}, \varepsilon_{22}, \varepsilon_{33}, 2\varepsilon_{23}, 2\varepsilon_{13}, 2\varepsilon_{12}]^T$, and the stress matrix $\boldsymbol{\sigma} = [\sigma_{11}, \sigma_{22}, \sigma_{33}, \sigma_{23}, \sigma_{13}, \sigma_{12}]^T$. The

302 6×6 fracture compliance matrix \mathbf{Z}_1 and additional dimensionless matrix \mathbf{Z}_2 according to the Voigt notation are defined as

$$303 \quad \mathbf{Z}_1 = \begin{bmatrix} 0 & 0 & 0 & 0 & 0 & 0 \\ 0 & 0 & 0 & 0 & 0 & 0 \\ 0 & 0 & \mathbf{Z}_W & 0 & 0 & 0 \\ 0 & 0 & 0 & \mathbf{Z}_T & 0 & 0 \\ 0 & 0 & 0 & 0 & \mathbf{Z}_T & 0 \\ 0 & 0 & 0 & 0 & 0 & 0 \end{bmatrix}, \quad \mathbf{Z}_2 = \begin{bmatrix} 0 & 0 & 0 & 0 & 0 & 0 \\ 0 & 0 & 0 & 0 & 0 & 0 \\ \mathbf{Z}_W & 0 & 0 & 0 & 0 & 0 \\ 0 & 0 & 0 & 0 & 0 & 0 \\ 0 & 0 & 0 & 0 & 0 & 0 \\ 0 & 0 & 0 & 0 & 0 & 0 \end{bmatrix}. \quad (20)$$

304 The average strain in a homogeneous porous rock containing single fracture can be expressed as the sum of the strains of
305 background and the fractures

306 $\hat{\boldsymbol{\epsilon}} = \hat{\boldsymbol{\epsilon}}^b + \hat{\boldsymbol{\epsilon}}^c. \quad (15)$

307 $\boldsymbol{\epsilon} = \boldsymbol{\epsilon}^b + \boldsymbol{\epsilon}^c. \quad (21)$

308 Substituting [equation \(12\)](#) and [\(13\)](#) into [equation \(15\)](#), [Eq. \(15\)](#) and [Eq. \(19\)](#) into [Eq. \(21\)](#), we can obtain the average strain
309 matrix

310 $\hat{\boldsymbol{\epsilon}} = \left[\hat{\mathbf{S}}^b + \frac{S}{V} (\hat{\mathbf{Z}}^1 + \hat{\mathbf{Z}}^H \hat{\mathbf{S}}^b) \right] \hat{\boldsymbol{\sigma}}. \quad (16)$

311 $\boldsymbol{\epsilon} = \left[\mathbf{S}^b + \frac{s}{V} (\mathbf{Z}_1 + \mathbf{Z}_2 \mathbf{S}^b) \right] \boldsymbol{\sigma}. \quad (22)$

312 Thus, the effective stiffness matrix \mathbf{C} can be expressed as

313 $\mathbf{C} = \left[\hat{\mathbf{S}}^b + \frac{S}{V} (\hat{\mathbf{Z}}^1 + \hat{\mathbf{Z}}^H \hat{\mathbf{S}}^b) \right]^{-1}. \quad (17)$

314 $\mathbf{C} = \left[\mathbf{S}^b + \frac{s}{V} (\mathbf{Z}_1 + \mathbf{Z}_2 \mathbf{S}^b) \right]^{-1} = \mathbf{C}^b \left[\mathbf{I} + \frac{s}{V} (\mathbf{Z}_1 \mathbf{C}^b + \mathbf{Z}_2) \right]^{-1}. \quad (23)$

315 The effective stiffness matrix of case of an inclined fracture can be obtained by rotating the coordinate axis to keep z -axis
316 perpendicular to fracture interface. We define the inclined fracture have an angle φ and an azimuth angle θ , and then the
317 rotation matrix can be obtained:

318 $\hat{\mathbf{R}} = \begin{bmatrix} \cos \theta \cos \varphi & -\sin \theta & \cos \theta \sin \varphi \\ \sin \theta \cos \varphi & \cos \theta & \sin \theta \sin \varphi \\ -\sin \varphi & 0 & \cos \varphi \end{bmatrix}, \quad (18)$

319 $\mathbf{R} = \begin{bmatrix} \cos \theta \cos \varphi & -\sin \theta & \cos \theta \sin \varphi \\ \sin \theta \cos \varphi & \cos \theta & \sin \theta \sin \varphi \\ -\sin \varphi & 0 & \cos \varphi \end{bmatrix}, \quad (24)$

320 as well as the corresponding stress Bond matrix $\hat{\mathbf{A}}_\sigma(\hat{\mathbf{R}})$ and strain Bond matrix $\hat{\mathbf{A}}_\epsilon(\hat{\mathbf{R}})$. The new stress matrix $\hat{\boldsymbol{\epsilon}}'$ and strain
321 matrix $\hat{\boldsymbol{\sigma}}'$ can be expressed as [the multiplication of the old one and Bond matrix](#):

322 $\hat{\boldsymbol{\epsilon}}' = \hat{\mathbf{A}}_\epsilon \hat{\boldsymbol{\epsilon}}, \quad \hat{\boldsymbol{\sigma}}' = \hat{\mathbf{A}}_\sigma \boldsymbol{\sigma}'. \quad (19)$

323 $\boldsymbol{\epsilon}' = \mathbf{A}_\epsilon \boldsymbol{\epsilon}, \quad \boldsymbol{\sigma}' = \mathbf{A}_\sigma \boldsymbol{\sigma}. \quad (25)$

324 By substituting [equation \(19\)](#) into [equation \(13\)](#), [Eq. \(25\)](#) into [Eq. \(19\)](#), the new exceed fracture strain matrix can be obtained

325 $\hat{\mathbf{\epsilon}}^c = \frac{S}{V} \hat{\mathbf{A}}_e \left(\hat{\mathbf{Z}}^I + \hat{\mathbf{Z}}^{II} \hat{\mathbf{S}}^b \right) \hat{\mathbf{A}}_e^T \hat{\mathbf{\sigma}}, \quad (20)$

326 $\mathbf{\epsilon}^e = \frac{s}{\psi} \mathbf{A}_e (\mathbf{Z}_1 + \mathbf{Z}_2 \mathbf{S}^b) \mathbf{A}_e^T \mathbf{\sigma}. \quad (26)$

327 Finally, substituting [equation \(12\)](#) and [\(20\)](#) into [equation \(15\)](#), [Eq. \(6\)](#) into [Eq. \(21\)](#), the average strain matrix of each numerical
328 cell containing discrete distributed fractures with the same arbitrary direction can be expressed as

329 $\hat{\mathbf{\epsilon}} = \left[\hat{\mathbf{S}}^b + \frac{S}{V} \hat{\mathbf{A}}_e \left(\hat{\mathbf{Z}}^I + \hat{\mathbf{Z}}^{II} \hat{\mathbf{S}}^b \right) \hat{\mathbf{A}}_e^T \right] \hat{\mathbf{\sigma}}. \quad (21)$

330 $\mathbf{\epsilon} = \left[\mathbf{S}^b + \frac{s}{\psi} \mathbf{A}_e (\mathbf{Z}_1 + \mathbf{Z}_2 \mathbf{S}^b) \mathbf{A}_e^T \right] \mathbf{\sigma}, \quad (27)$

331 and the corresponding effective stiffness matrix \mathbf{C} is

332 $\mathbf{C} = \left[\hat{\mathbf{S}}^b + \frac{S}{V} \hat{\mathbf{A}}_e \left(\hat{\mathbf{Z}}^I + \hat{\mathbf{Z}}^{II} \hat{\mathbf{S}}^b \right) \hat{\mathbf{A}}_e^T \right]^{-1}. \quad (22)$

333 $\mathbf{C} = \left[\mathbf{S}^b + \frac{s}{\psi} \mathbf{A}_e (\mathbf{Z}_1 + \mathbf{Z}_2 \mathbf{S}^b) \mathbf{A}_e^T \right]^{-1}, \quad (28)$

334 If the background media is isotropic, the \mathbf{C} can be simplified as

335 $\mathbf{C} = \mathbf{C}^{iso} \left[\mathbf{I} + \frac{S}{V} \hat{\mathbf{A}}_e \left(\hat{\mathbf{Z}}^I \mathbf{C}^{iso} + \hat{\mathbf{Z}}^{II} \right) \hat{\mathbf{A}}_e^T \right]^{-1}. \quad (23)$

336 $\mathbf{C} = \mathbf{C}^b \left[\mathbf{I} + \frac{s}{\psi} \mathbf{A}_e (\mathbf{Z}_1 \mathbf{C}^b + \mathbf{Z}_2) \mathbf{A}_e^T \right]^{-1}, \quad (29)$

337 If we ignore the interaction between different fractures and the FPD along the fracture interfaces, the result can be easily
338 extended to the case of multiple sets of discrete distributed large-scale fractures with arbitrary orientation:

339 $\mathbf{C} = \mathbf{C}^{iso} \left[\mathbf{I} + \sum_{r=1}^{N_c} \frac{S_r}{V} \hat{\mathbf{A}}_{er} \left(\hat{\mathbf{Z}}_r^I \mathbf{C}_r^{iso} + \hat{\mathbf{Z}}_r^{II} \right) \hat{\mathbf{A}}_{er}^T \right]^{-1}. \quad (24)$

340 $\mathbf{C} = \mathbf{C}^b \left[\mathbf{I} + \sum_{r=1}^{N_c} \frac{s_r}{\psi} \mathbf{A}_{er} (\mathbf{Z}_{1r} \mathbf{C}^b + \mathbf{Z}_{2r}) \mathbf{A}_{er}^T \right]^{-1}, \quad (30)$

341 where N_c is total number of the fracture directions and the subscript r denotes the r th direction. The derived effective stiffness
342 matrix is to be employed in the viscoelastic finite-difference modeling of discrete distributed large-scale fractures in porous
343 rock.

344 [Since the local effective medium theory assumes that the real structure of the fractured porous rock is substituted by ideal](#)
345 [continua, the balance equations of classical continuum mechanics can be applied without considering the discontinuity at the](#)
346 [fracture interfaces, and the constitutive equations can be characterized by the effective viscoelastic stiffness. Combined with](#)
347 [the effective complex-valued and frequency-dependent TTI viscoelastic stiffness, the 2-D frequency-domain second-order](#)
348 [heterogeneous governing equations with perfectly matched layer \(PML\) of fractured porous rock can be expressed as:](#)

349 **5. Seismic modeling of fractured porous rock**

350 In this section, we focus on the implementation of seismic modeling of fluid saturated porous media containing discrete
 351 distributed large scale fractures in 2D case. We develop a viscoelastic modeling scheme based on the VLSM and local effective
 352 medium theory (Coates and Schoenberg, 1995) to incorporate the FPD effects between fractures and background. To validate
 353 that the proposed viscoelastic modeling scheme can capture the impact of FPD effects on seismic wave scattering of fractures,
 354 we outline the implementation of poroelastic modeling scheme using an explicit application of the PLSM.

355 **5.1 viscoelastic modeling based on VLSM**

356 For viscoelastic modeling, we adopt local effective media theory based on VLSM to derive the effective anisotropic
 357 viscoelastic compliances in each numerical cell by superimposing the compliances of the background and the fractures. Since
 358 the real structure of the rock is substituted by ideally continua, the balance equations of classical continuum mechanics can be
 359 applied without considering the discontinuity at the fracture interfaces (Lewis and Schrefler, 1998; Gavagnin et al., 2020), and
 360 the constitutive equations are characterized by effective complex valued and frequency dependent TTI viscoelastic stiffness.
 361 Thus, the second order heterogeneous governing equations of fractured porous rock with PML in frequency domain can be
 362 expressed as:

$$363 \omega^2 \rho u_x + \frac{1}{\xi_x} \partial_x \left(\frac{c_{11}}{\xi_x} \partial_x u_x + \frac{c_{13}}{\xi_z} \partial_z u_z + \frac{c_{15}}{\xi_z} \partial_z u_x + \frac{c_{15}}{\xi_x} \partial_x u_z \right) + \frac{1}{\xi_z} \partial_z \left(\frac{c_{15}}{\xi_x} \partial_x u_x + \frac{c_{35}}{\xi_z} \partial_z u_z + \frac{c_{55}}{\xi_z} \partial_z u_x + \frac{c_{55}}{\xi_x} \partial_x u_z \right) = 0, \quad (25)$$

$$\omega^2 \rho u_z + \frac{1}{\xi_x} \partial_x \left(\frac{c_{15}}{\xi_x} \partial_x u_x + \frac{c_{35}}{\xi_z} \partial_z u_z + \frac{c_{55}}{\xi_z} \partial_z u_x + \frac{c_{55}}{\xi_x} \partial_x u_z \right) + \frac{1}{\xi_z} \partial_z \left(\frac{c_{13}}{\xi_x} \partial_x u_x + \frac{c_{33}}{\xi_z} \partial_z u_z + \frac{c_{35}}{\xi_z} \partial_z u_x + \frac{c_{35}}{\xi_x} \partial_x u_z \right) = 0,$$

$$364 \omega^2 \rho u_x + \frac{1}{\xi_x} \partial_x \left(\frac{c_{11}}{\xi_x} \partial_x u_x + \frac{c_{13}}{\xi_z} \partial_z u_z + \frac{c_{15}}{\xi_z} \partial_z u_x + \frac{c_{15}}{\xi_x} \partial_x u_z \right) + \frac{1}{\xi_z} \partial_z \left(\frac{c_{15}}{\xi_x} \partial_x u_x + \frac{c_{35}}{\xi_z} \partial_z u_z + \frac{c_{55}}{\xi_z} \partial_z u_x + \frac{c_{55}}{\xi_x} \partial_x u_z \right) = 0, \quad (31a)$$

$$365 \omega^2 \rho u_z + \frac{1}{\xi_x} \partial_x \left(\frac{c_{13}}{\xi_x} \partial_x u_x + \frac{c_{35}}{\xi_z} \partial_z u_z + \frac{c_{55}}{\xi_z} \partial_z u_x + \frac{c_{55}}{\xi_x} \partial_x u_z \right) + \frac{1}{\xi_z} \partial_z \left(\frac{c_{13}}{\xi_x} \partial_x u_x + \frac{c_{33}}{\xi_z} \partial_z u_z + \frac{c_{35}}{\xi_z} \partial_z u_x + \frac{c_{35}}{\xi_x} \partial_x u_z \right) = 0, \quad (31b)$$

366 where u_x and u_z are the horizontal and vertical components of particle displacement vector, ρ is the effective density, and c_{ij}
 367 are the components of complex-valued and frequency-dependent effective stiffness matrix, ξ_x and ξ_z are the frequency domain
 368 PML damping functions.

369 where u_x and u_z are the horizontal and vertical components of particle displacement vector, ρ is the effective density, and
 370 c_{ij} are the components of complex valued and frequency dependent effective stiffness matrix, ξ_x and ξ_z are the frequency
 371 domain PML damping functions.

372 In time domain, the governing equations are integral differential equations, which require special processing for the
 373 convolution operations, resulting in high computational costs. Although the problem can be relieved by memory functions, it
 374 still requires high memory requirements. Instead, the governing equations can be straightforwardly solved using FDFD. To
 375 efficiently and accurately modelling of seismic wave propagation in fluid saturated fractured porous rock, we solve the second-

376 order heterogeneous governing equations with mixed-grid stencil FDFD method (Jo et al., 1996; Hustedt et al. 2004). The
 377 mixed system of governing equations is formulated by combining the classical Cartesian coordinate system (CS) and the 45°-
 378 rotated coordinate system (RS):

$$\begin{aligned} 379 \quad \omega^2 \rho u_x + w_1 (A_c u_x + B_c u_z) + (1-w_1) (A_r u_x + B_r u_z) &= 0, \\ \omega^2 \rho u_z + w_1 (C_c u_x + D_c u_z) + (1-w_1) (C_r u_x + D_r u_z) &= 0, \end{aligned} \quad (26)$$

$$380 \quad \omega^2 \rho u_x + w_1 (A_c u_x + B_c u_z) + (1-w_1) (A_r u_x + B_r u_z) = 0, \quad (32a)$$

$$381 \quad \omega^2 \rho u_z + w_1 (C_c u_x + D_c u_z) + (1-w_1) (C_r u_x + D_r u_z) = 0, \quad (32b)$$

382 where the optimal averaging coefficient $w_1 = 0.5461$ (Jo et al., 1996). The coefficients A_c, B_c, C_c, D_c and A_r, B_r, C_r, D_r are
 383 functions of the damping functions, effective stiffness coefficients and spatial derivative operators and the detailed expressions
 384 are given in Appendix A. We follow Hustedt et al., (2004) and Liu et al., (2018) to discretize the derivative operation on the
 385 mixed systems using mixed grid stencil. After discretization and arrangement, the mixed system of governing equations can
 386 be written in matrix form as

$$387 \quad \begin{bmatrix} \mathbf{M} + w_1 \mathbf{A}_c + (1-w_1) \mathbf{A}_r & w_1 \mathbf{B}_c + (1-w_1) \mathbf{B}_r \\ w_1 \mathbf{C}_c + (1-w_1) \mathbf{C}_r & \mathbf{M} + w_1 \mathbf{D}_c + (1-w_1) \mathbf{D}_r \end{bmatrix} \begin{bmatrix} \mathbf{u}_x \\ \mathbf{u}_z \end{bmatrix} = \begin{bmatrix} \mathbf{0} \\ \mathbf{0} \end{bmatrix}, \quad (27)$$

$$388 \quad \begin{bmatrix} \mathbf{M} + w_1 \mathbf{A}_e + (1-w_1) \mathbf{A}_f & w_1 \mathbf{B}_e + (1-w_1) \mathbf{B}_f \\ w_1 \mathbf{C}_e + (1-w_1) \mathbf{C}_f & \mathbf{M} + w_1 \mathbf{D}_e + (1-w_1) \mathbf{D}_f \end{bmatrix} \begin{bmatrix} \mathbf{u}_x \\ \mathbf{u}_z \end{bmatrix} = \begin{bmatrix} \mathbf{0} \\ \mathbf{0} \end{bmatrix}, \quad (36)$$

389 where \mathbf{M} denotes the diagonal mass matrix of coefficients $\omega^2 \rho$, and blocks $\mathbf{A}_c, \mathbf{B}_c, \mathbf{C}_c, \mathbf{D}_c$ and $\mathbf{A}_r, \mathbf{B}_r, \mathbf{C}_r, \mathbf{D}_r$ form the
 390 stiffness matrices for the CS and RS stencils, respectively, and the corresponding coefficients of submatrices are given in
 391 Appendix B.

392 To improve the modelling accuracy of mixed-grid stencil, the acceleration term $\omega^2 \rho$ are approximated using a weighted
 393 average over the mixed operator stencil nodes:

$$394 \quad [\omega^2 \rho]_{i,j} \approx \omega^2 \left[w_{m1} \rho_{i,j} + w_{m2} (\rho_{i+1,j} + \rho_{i-1,j} + \rho_{i,j+1} + \rho_{i,j-1}) + w_{m3} (\rho_{i+1,j+1} + \rho_{i-1,j-1} + \rho_{i-1,j+1} + \rho_{i+1,j-1}) \right], \quad (28)$$

$$395 \quad [\omega^2 \rho]_{i,j} \approx \omega^2 \left[w_{m1} \rho_{i,j} + w_{m2} (\rho_{i+1,j} + \rho_{i-1,j} + \rho_{i,j+1} + \rho_{i,j-1}) + \frac{(1-w_{m1}-4w_{m2})}{4} (\rho_{i+1,j+1} + \rho_{i-1,j-1} + \rho_{i-1,j+1} + \rho_{i+1,j-1}) \right], \quad (37)$$

396 where the optimal coefficients $w_{m1} = 0.6248$, $w_{m2} = 0.09381$ and $w_{m3} = (1-w_{m1}-4w_{m2})/4$ are computed by Jo et al. (1996).

397 In order to assess the FPD effects on seismic response, a similar procedure can be adopted in the implementation of elastic
 398 modeling by replacing the frequency-dependent fracture compliances with its low- or high-frequency limit compliances. The
 399 main advantage of our VLSM-based modeling scheme over poroelastic modeling schemes is that the fractured domain can be
 400 modeled using a viscoelastic solid, while the rest of the domain can be modeled using an elastic solid.

401 In order to assess the FPD effects on seismic response, the similar procedure was adopted in the implementation of elastic
 402 modeling by replacing the VLSM with the LFLSM (assuming fluid pressure is equilibrium) or the HFLSM (assuming fluid
 403 pressure is unequilibrium).

404 **3.2 Poroelastic modeling based on PLSM**

405 **5.2 Poroelastic modeling based on PLSM**

406 The poroelastic modeling means that we numerically solve the Biot's equations and adopt an explicit implementation of the
 407 PLSM across each fracture instead of using the effective media theory. Hence, the poroelastic modeling can naturally deal with
 408 the FPD between fracture and background and account for its impact on wave scattering. To verify the effectiveness of the

409 viscoelastic modeling based on VLSM, we compared the results obtained from viscoelastic scheme with those obtained from

410 the poroelastic scheme. Although it is difficult to implement an explicit application of PLSM for arbitrary orientated fracture,
 411 it is relatively straightforward for horizontal or vertical fracture. In the following text, we outline the poroelastic modeling for
 412 a single horizontal fracture embedded in an isotropic homogeneous background with an explicit implementation of the PLSM.

413 In frequency domain, the governing equations for an isotropic poroelastic media in the absent of fractures can be written as

414 (Biot, 1962):

$$415 \begin{aligned} -\omega^2 \rho u_i - \omega^2 \rho_f w_i &= \partial_i \sigma_{ij}, \\ -\omega^2 \rho_f u_i - \omega^2 \rho_w w_i + i\omega \frac{\eta}{\kappa} w_i &= -\partial_i P_f, \\ \sigma_{ij} &= (H_u - 2\mu) \partial_i u_i + \alpha M \partial_i w_i + \mu (\partial_j u_i + \partial_i u_j), \\ -P_f &= \alpha M \partial_i u_i + M \partial_i w_i. \end{aligned} \quad (29)$$

416 In the presence of fractures, the spatial derivative of stress remains unchanged. However, due to the discontinuity of particle
 417 displacements across the fracture interface, its spatial derivative consists of two parts, i.e. the background and the fracture:

$$418 \begin{aligned} \frac{\partial u_x}{\partial z} &= \left(\frac{\partial u_x}{\partial z} \right)_{BG} + \left(\frac{\partial u_x}{\partial z} \right)_{FR}, \\ \frac{\partial u_z}{\partial z} &= \left(\frac{\partial u_z}{\partial z} \right)_{BG} + \left(\frac{\partial u_z}{\partial z} \right)_{FR}, \\ \frac{\partial w_z}{\partial z} &= \left(\frac{\partial w_z}{\partial z} \right)_{BG} + \left(\frac{\partial w_z}{\partial z} \right)_{FR}. \end{aligned} \quad (30)$$

419 The spatial derivative of the background is described by the equation (29):

$$420 \begin{aligned} \left(\frac{\partial u_x}{\partial z} \right)_{BG} &= \frac{H_D}{4\mu(H_D - \mu)} \sigma_{xx} - \frac{H_D - 2\mu}{4\mu(H_D - \mu)} \sigma_{zz} + \frac{2\alpha\mu}{4\mu(H_D - \mu)} P_f, \\ \left(\frac{\partial u_z}{\partial z} \right)_{BG} &= -\frac{H_D - 2\mu}{4\mu(H_D - \mu)} \sigma_{xx} + \frac{H_D}{4\mu(H_D - \mu)} \sigma_{zz} + \frac{2\alpha\mu}{4\mu(H_D - \mu)} P_f, \\ \left(\frac{\partial w_x}{\partial z} + \frac{\partial w_z}{\partial z} \right)_{BG} &= -\frac{2\alpha\mu}{4\mu(H_D - \mu)} \sigma_{xx} - \frac{2\alpha\mu}{4\mu(H_D - \mu)} \sigma_{zz} - \frac{H_u - \mu}{M(H_D - \mu)} P_f. \end{aligned} \quad (31)$$

421 The fracture induced spatial derivative can be obtained based on the PLSM:

$$\begin{aligned}
 \left(\frac{\partial u_x}{\partial z} \right)_{FR} &= \frac{\Delta u_x}{\Delta z} = \frac{Z_T}{\Delta z} \sigma_{xz}, \\
 \left(\frac{\partial u_z}{\partial z} \right)_{FR} &= \frac{\Delta u_z}{\Delta z} = \frac{Z_{N_D}}{\Delta z} (\sigma_{zz} + \alpha P_f), \\
 \left(\frac{\partial w_z}{\partial z} \right)_{FR} &= \frac{\Delta w_z}{\Delta z} = -\frac{Z_{N_D}}{\Delta z} \left(\alpha \sigma_{zz} + \frac{H_U}{M} P_f \right).
 \end{aligned}
 \quad (32)$$

423 By substituting equation (31)-(32) into equation (30) and rewritten equation (29), we obtain the governing equations for
 424 numerical simulation of elastic wave in fractured poroelastic media in matrix form:

$$- \omega^2 \hat{\mathbf{R}} \hat{\mathbf{u}} = \nabla \hat{\mathbf{S}}^{-1} \nabla^T \hat{\mathbf{u}}, \quad (33)$$

426 where $\hat{\mathbf{u}} = (u_x, u_z, w_x, w_z)^T$ is the displacement vector, $\hat{\mathbf{R}}$, $\hat{\mathbf{S}}$ and ∇ are the density, compliance and spatial derivative matrix,
 427 respectively. The three matrices in equation (33) are defined as:

$$\hat{\mathbf{R}} = \begin{bmatrix} \rho & 0 & \rho_f & 0 \\ 0 & \rho & 0 & \rho_f \\ \rho_f & 0 & \rho_m & 0 \\ 0 & \rho_f & 0 & \rho_m \end{bmatrix}, \quad \left(\rho_m = \rho_w - \frac{i\eta}{\omega\kappa} \right). \quad (34)$$

$$\nabla = \begin{bmatrix} \partial_x & 0 & \partial_z & 0 \\ 0 & \partial_z & \partial_x & 0 \\ 0 & 0 & 0 & \partial_x \\ 0 & 0 & 0 & \partial_z \end{bmatrix}, \quad (35)$$

$$\hat{\mathbf{S}} = \begin{bmatrix} \frac{H_D}{4\mu(H_D - \mu)} & -\frac{H_D - 2\mu}{4\mu(H_D - \mu)} & 0 & -\frac{2\alpha\mu}{4\mu(H_D - \mu)} \\ -\frac{H_D - 2\mu}{4\mu(H_D - \mu)} & \frac{H_D}{4\mu(H_D - \mu)} + \frac{Z_{N_D}}{\Delta z} & 0 & -\frac{2\alpha\mu}{4\mu(H_D - \mu)} - \frac{\alpha Z_{N_D}}{\Delta z} \\ 0 & 0 & \frac{1}{\mu} + \frac{Z_T}{\Delta z} & 0 \\ -\frac{2\alpha\mu}{4\mu(H_D - \mu)} - \frac{2\alpha\mu}{4\mu(H_D - \mu)} - \frac{\alpha Z_{N_D}}{\Delta z} & 0 & -\frac{H_U - \mu}{M(H_D - \mu)} - \frac{H_U Z_{N_D}}{M\Delta z} & \end{bmatrix}. \quad (36)$$

431 A compact discretized wave equation system that contains only displacement field can be obtained by using second-order
 432 difference operators to discretize the new governing equations:

$$\begin{bmatrix} \mathbf{G}_{11} & \mathbf{G}_{12} & \mathbf{G}_{13} & \mathbf{G}_{14} \\ \mathbf{G}_{21} & \mathbf{G}_{22} & \mathbf{G}_{23} & \mathbf{G}_{24} \\ \mathbf{G}_{31} & \mathbf{G}_{32} & \mathbf{G}_{33} & \mathbf{G}_{34} \\ \mathbf{G}_{41} & \mathbf{G}_{42} & \mathbf{G}_{43} & \mathbf{G}_{44} \end{bmatrix} \begin{bmatrix} \mathbf{u}_x \\ \mathbf{u}_z \\ \mathbf{w}_x \\ \mathbf{w}_z \end{bmatrix} = \begin{bmatrix} \mathbf{0} \\ \mathbf{0} \\ \mathbf{0} \\ \mathbf{0} \end{bmatrix}, \quad (37)$$

434 where blocks $\mathbf{G}_{i,j}$ ($i, j = 1 \dots 4$) forms the stiffness matrices of the discretized system of the poroelastic wave equations. The
 435 poroelastic modeling based on PLSM will be used to validate the other modeling schemes $\omega^2 \rho \mathbf{u} + \omega^2 \rho_f \mathbf{w} + \nabla \cdot \boldsymbol{\sigma} = 0$,
 436

$$(38a)$$

437 $\omega^2 \rho_f u + i\omega \frac{\eta}{\kappa} w - \nabla p_f = 0, \quad (38b)$

438 $\sigma = [(H_u - 2\mu) \nabla \cdot \mathbf{u} + \alpha M \nabla \cdot \mathbf{w}] \mathbf{I} + \mu (\nabla \mathbf{u} + \nabla \mathbf{u}^T), \quad (38c)$

439 $-p_f = \alpha M \nabla \cdot \mathbf{u} + M \nabla \cdot \mathbf{w}. \quad (38d)$

440 By discretizing Eqs. (38a)–(38d) using second order differences, we can obtain:

441 $\omega^2 \rho_f u_{x,i,j} + \omega^2 \rho_f w_{x,i,j} + \frac{\sigma_{xx,i+1,j} - \sigma_{xx,i,j}}{\Delta} + \frac{\sigma_{xz,i,j+1} - \sigma_{xz,i,j}}{\Delta} = 0, \quad (39a)$

442 $\omega^2 \rho_f u_{x,i,j} + \omega^2 \rho_f w_{x,i,j} + \frac{\sigma_{xx,i+1,j} - \sigma_{xx,i,j}}{\Delta} + \frac{\sigma_{xz,i,j+1} - \sigma_{xz,i,j}}{\Delta} = 0, \quad (39b)$

443 $\omega^2 \rho_f u_{x,i,j} + i\omega \frac{\eta}{\kappa} w_{x,i,j} - \frac{p_{f,i+1,j} - p_{f,i,j}}{\Delta} = 0, \quad (39c)$

444 $\omega^2 \rho_f u_{z,i,j} + i\omega \frac{\eta}{\kappa} w_{z,i,j} - \frac{p_{f,i,j+1} - p_{f,i,j}}{\Delta} = 0, \quad (39d)$

445 $\sigma_{xx,i,j} = H_u \frac{u_{x,i+1,j} - u_{x,i,j}}{\Delta} + (H_u - 2\mu) \frac{u_{z,i,j+1} - u_{z,i,j}}{\Delta} + \alpha M \left(\frac{w_{x,i+1,j} - w_{x,i,j}}{\Delta} + \frac{w_{z,i,j+1} - w_{z,i,j}}{\Delta} \right), \quad (39e)$

446 $\sigma_{zz,i,j} = (H_u - 2\mu) \frac{u_{x,i+1,j} - u_{x,i,j}}{\Delta} + H_u \frac{u_{z,i,j+1} - u_{z,i,j}}{\Delta} + \alpha M \left(\frac{w_{x,i+1,j} - w_{x,i,j}}{\Delta} + \frac{w_{z,i,j+1} - w_{z,i,j}}{\Delta} \right), \quad (39f)$

447 $\sigma_{xz,i,j} = \mu \left(\frac{u_{x,i+1,j} - u_{x,i,j}}{\Delta} + \frac{u_{z,i,j+1} - u_{z,i,j}}{\Delta} \right), \quad (39g)$

448 $-p_f = \alpha M \frac{u_{x,i+1,j} - u_{x,i,j}}{\Delta} + \alpha M \frac{u_{z,i,j+1} - u_{z,i,j}}{\Delta} + M \left(\frac{w_{x,i+1,j} - w_{x,i,j}}{\Delta} + \frac{w_{z,i,j+1} - w_{z,i,j}}{\Delta} \right). \quad (39h)$

449 In the presence of horizontal fracture passing through the numerical cell (i, j_0) , the PLSM can be written as:

450 $u_{x,i,j_0+1} - u_{x,i,j_0} = (Z_T \sigma_{xz})_{i,j_0}, \quad (40a)$

451 $u_{z,i,j_0+1} - u_{z,i,j_0} = (Z_{ND} \sigma_{zz} + Z_{ND} \alpha p_f)_{i,j_0}, \quad (40b)$

452 $w_{z,i,j_0+1} - w_{z,i,j_0} = -\left(\alpha Z_{ND} \sigma_{zz} + \frac{\alpha Z_{ND}}{B} p_f \right)_{i,j_0}. \quad (40c)$

453 Rearrange the Eqs. (39e)–(39h), i.e. use the displacement components to represent the stress components, and superimpose the

454 discrete Eqs. (40a)–(40c), we get the following discrete equations:

455 $\frac{u_{x,i+1,j_0} - u_{x,i,j_0}}{\Delta} = \left[\frac{H_D}{4\mu(H_D - \mu)} \sigma_{xx} + \frac{(2\mu - H_D)}{4\mu(H_D - \mu)} \sigma_{zz} + \frac{2\alpha\mu}{4\mu(H_D - \mu)} p_f \right]_{i,j_0}, \quad (41a)$

456 $\frac{u_{z,i+1,j_0} - u_{z,i,j_0}}{\Delta} = \left[\frac{(2\mu - H_D)}{4\mu(H_D - \mu)} \sigma_{xx} + \left[\frac{H_D}{4\mu(H_D - \mu)} + \frac{Z_{ND}}{\Delta} \right] \sigma_{zz} + \left[\frac{2\alpha\mu}{4\mu(H_D - \mu)} + \frac{\alpha Z_{ND}}{\Delta} \right] p_f \right]_{i,j_0}, \quad (41b)$

457 $\frac{u_{x,i,j_0+1} - u_{x,i,j_0}}{\Delta} + \frac{u_{z,i,j_0+1} - u_{z,i,j_0}}{\Delta} = \left[\left(\frac{1}{\mu} + \frac{Z_T}{\Delta} \right) \sigma_{xz} \right]_{i,j_0}, \quad (41c)$

458 $\frac{w_{x,i+1,j_0} - w_{x,i,j_0}}{\Delta} + \frac{w_{z,i+1,j_0} - w_{z,i,j_0}}{\Delta} = \left[\frac{2\alpha\mu}{4\mu(H_D - \mu)} \sigma_{xx} + \left(\frac{2\alpha\mu}{4\mu(H_D - \mu)} - \frac{\alpha Z_{ND}}{\Delta} \right) \sigma_{zz} - \frac{1}{M} \left(\frac{H_u - \mu}{H_D - \mu} + \frac{H_u Z_{ND}}{\Delta} \right) p_f \right]_{i,j_0}. \quad (41d)$

459 For a numerical cell, if $j \neq j_0$, we set $Z_{ND} = Z_T = 0$. By re-injecting Eqs. (41a)–(41d) into the discretized Eqs. (39a)–(39c),
460 we eliminate the stress terms and obtain the compact discretized system of wave equations that contain only the displacement
461 field:

$$\begin{bmatrix}
 G_{11} & G_{12} & G_{13} & G_{14} \\
 G_{21} & G_{22} & G_{23} & G_{24} \\
 G_{31} & G_{32} & G_{33} & G_{34} \\
 G_{41} & G_{42} & G_{43} & G_{44}
 \end{bmatrix}
 \begin{bmatrix}
 u_x \\
 u_z \\
 w_x \\
 w_z
 \end{bmatrix}
 = \begin{bmatrix}
 0 \\
 0 \\
 0 \\
 0
 \end{bmatrix}, \quad (42)$$

where blocks G_{ij} ($i, j = 1 \dots 4$) form the stiffness matrices of the discretized system of the poroelastic wave equations. The poroelastic modeling based on PLSM will be used to validate the other modeling schemes.

6.4 Numerical examples

Table1 Physical Properties of the Materials Employed in the Numerical Modeling

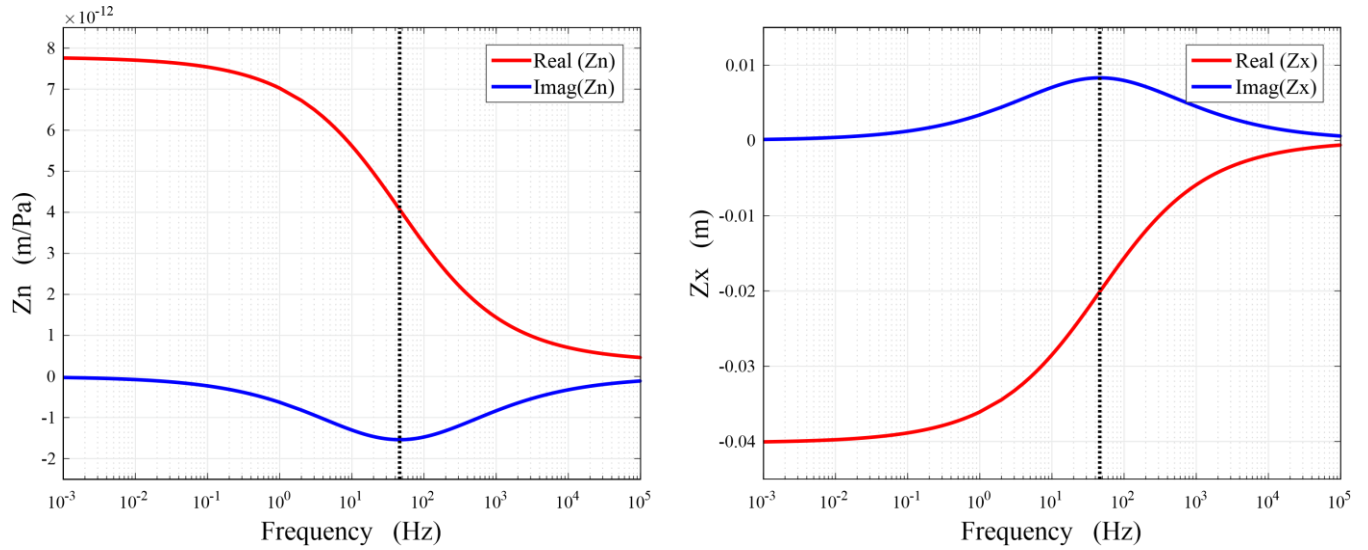
Parameters	Background	Fracture	Underlying
Porosity, ϕ	0.15	0.8	0.05
Permeability, κ	0.1 D	100 D	0.01 D
Solid bulk modulus, K_s	36 GPa	36 GPa	36 GPa
Frame bulk modulus, K_m	20.3 GPa	0.055 GPa	30.6 GPa
Frame shear modulus, μ_m	18.6 GPa	0.033 GPa	32.2 GPa
Solid density, ρ_s	2700 kg/m ³	2700 kg/m ³	2700 kg/m ³
Fluid density, ρ_f	1000 kg/m ³	1000 kg/m ³	1000 kg/m ³
Fluid shear viscosity, η_f	0.01 Poise	0.01 Poise	0.01 Poise
Fluid bulk modulus, K_f	2.25 GPa	2.25 GPa	2.25 GPa
Thickness, h		1 mm	

In this section, we apply different numerical modeling schemes on three fractured models to examine the FPD effects on seismic wave scattering. We mainly focus on the amplitudes and phases of the scattered and reflected waves generated by pressure source and shearing source.

4.1 Single fracture model

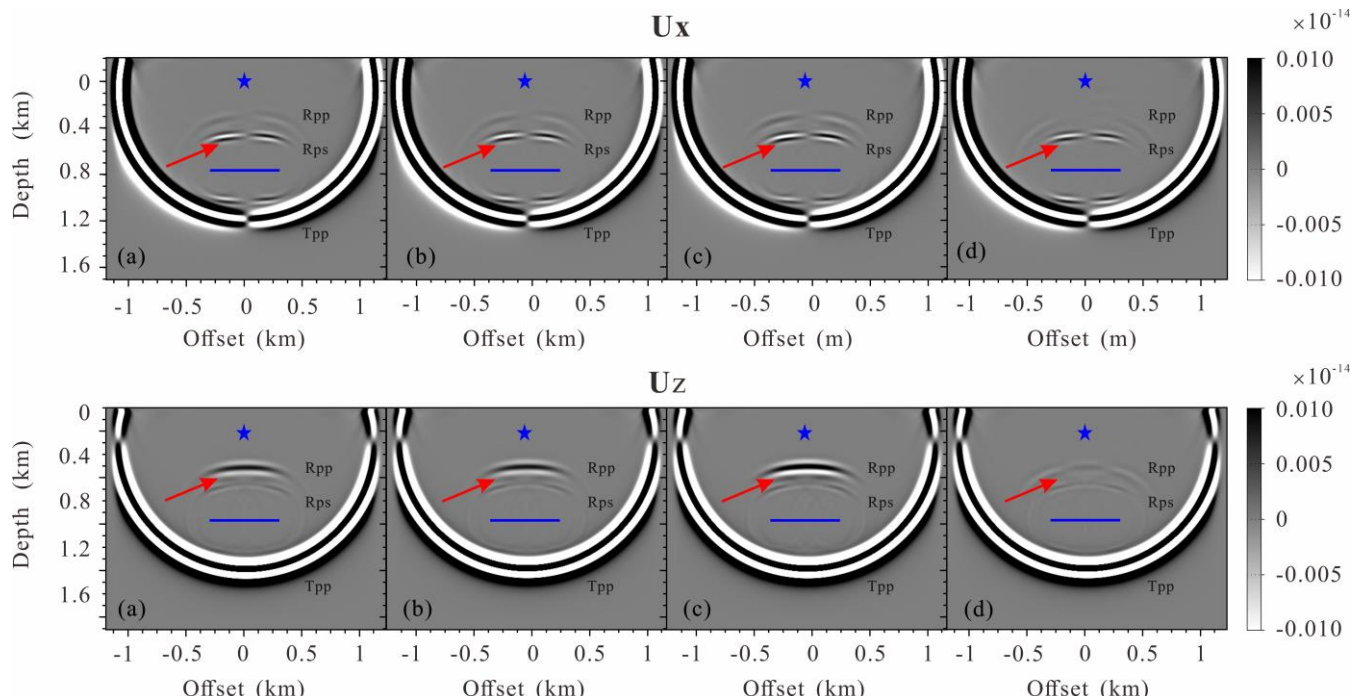
6.1 Single horizontal fracture model

Here, we numerically simulate the scattering of seismic waves from a single fracture embedded in a homogeneous background. The model measures 2000m×1500m with a grid interval 5m (namely, the numerical grids size is 401×301) surrounded by a 200m thick PML boundary. The fracture is parallel to the x -axis (a horizontal fracture) and located 750m directly below the source (1000m, 30m), with a 500m horizontal extending. The fracture is located 750m directly below the source (1000m, 30m), with a 500m horizontal extending. A Ricker wavelet with a central frequency of 35Hz is used as the temporal source excitation. The material properties of the fracture and background are given in Table 1 modified from Nakagawa and Schoenberg (2007) and Barbosa et al. (2016a). For comparison, we present the seismic wavefields obtained using the poroelastic modeling based on PLSM, the viscoelastic modeling based on VLSM, as well as the elastic modeling based on low-frequency limit of VLSM (LVLSM) and high-frequency limit of VLSM (HVLSM). For the convenience of observation of the impact of the FPD on the scattered P - and S -wave of the fracture, we apply the pressure source in all four schemes.



481
482 **Figure 1: Complex-valued and frequency-dependent Z_N and Z_X . The dashed vertical line denotes the characteristic frequency**
483 **computed using equation (8).**

484 ~~For comparison, we present the seismic wavefields obtained using the poroelastic modeling based on PLSM, the viscoelastic~~
485 ~~modeling based on VLSM, as well as the elastic modeling based on LFLSM and HFLSM. To further study the impact of FPD~~
486 ~~effects on P- and S-wave, we also apply the pressure source and shearing source in all four schemes, respectively.~~



487
488 **Figure 2: Snapshots of the wavefields components U_x and U_z for a single horizontal fracture model at 280ms: (a) the PLSM based**
489 **poroelastic modeling, (b) the VLSM based viscoelastic modeling, (c) the LVLSM based elastic modeling and (d) the HVLSM based**
490 **elastic modeling. The blue asterisk and line represent the source and the fracture, respectively.**

491 ~~Figure 1: Snapshots of the wavefields components U_x and U_z for a single horizontal fracture model at 280ms due to a P-wave point~~
492 ~~source: (a) the PLSM-based poroelastic modeling, (b) the VLSM-based viscoelastic modeling, (c) the LFLSM-based elastic modeling~~
493 ~~and (d) the HFLSM-based elastic modeling.~~

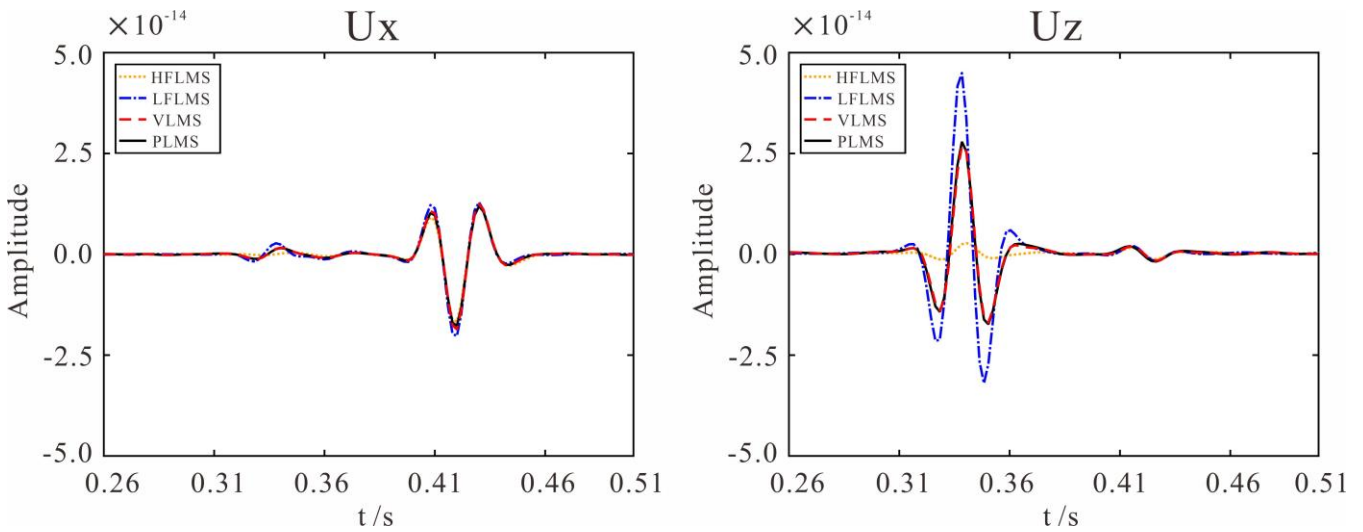


Figure 3: Comparison of 1-D seismograms components U_x and U_z at (1200m, 0m) for a single horizontal fracture model.

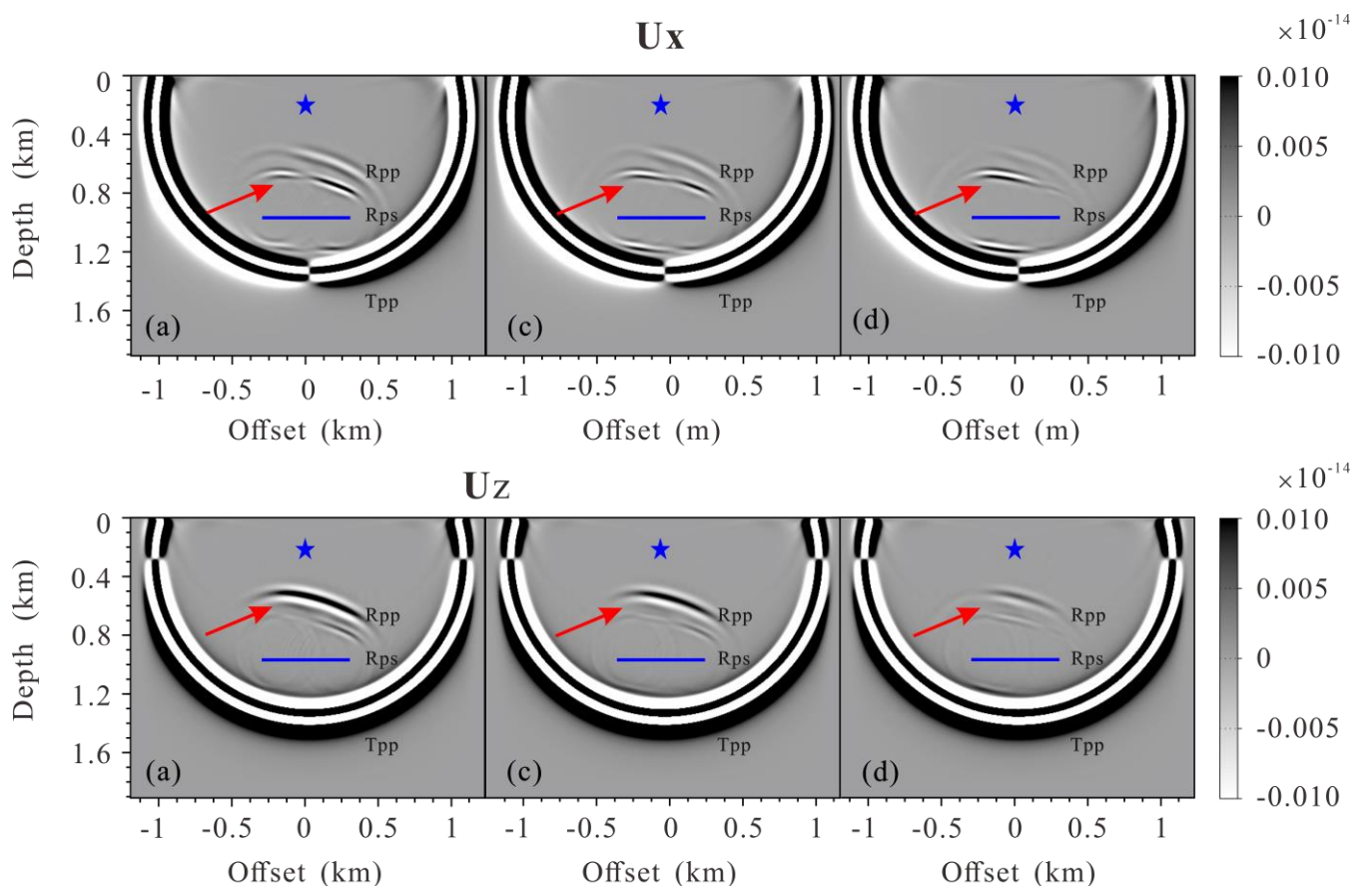
Figure 1 shows the complex-valued and frequency-dependent fracture normal compliance Z_n and dimensionless parameter Z_x computed from equation (6). The mechanical compliance of the fracture is strongly controlled by FPD effects. It can be observed that the real part of the fracture normal compliance decreases with the increment of frequency, while the imaginary part has a peak at the characteristic frequency, corresponding to the maximal dispersion. The central frequency (35Hz) of the Ricker wavelet used for numerical simulation is close to the characteristic frequency (46Hz), which ensures that the impact of the FDP effects on seismic scattering is significant in the seismic frequency band.

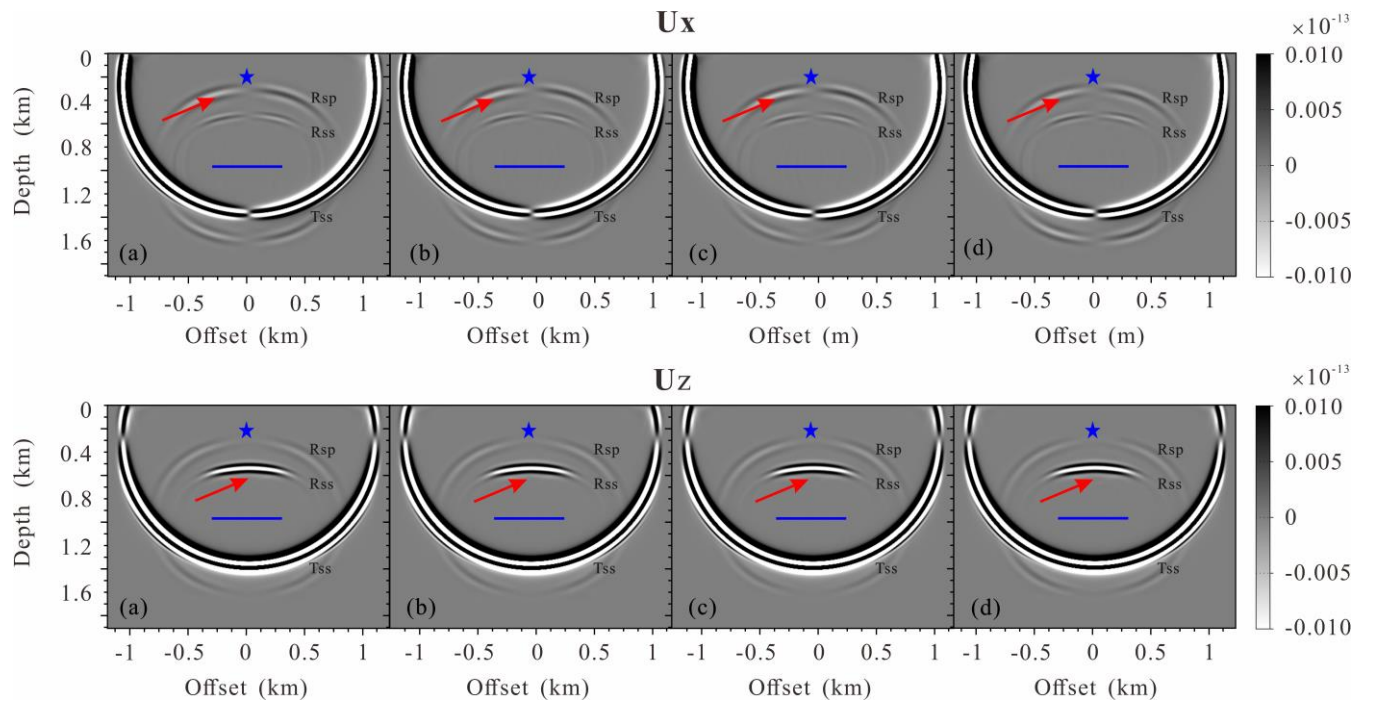
Figure 2: Comparison of 1-D seismograms components U_x and U_z at (1200m, 0m) for a single horizontal fracture model due to a P-wave point source.

Figure 4-2 shows the 280ms snapshots of the displacement fields for the single horizontal fracture model models with P-wave point source. The displacement fields are calculated by the PLSM-based poroelastic modeling, the VLSM-based viscoelastic modeling, the LFLSM-LVLSM-based elastic modeling and the HFLSM-HVLSM-based elastic modeling, respectively. The asterisk represents the source and the blue line represents the fracture. To make the small scattered wave visible, large amplitude is clipped, thus the transmitted compressional wave (T_{PP}), scattered compressional wave (S_{PP}) and scattered converted wave (S_{PS}) can be seen clearly. It should note that the slow P-waves are invisible in the poroelastic modeling, due to the high diffusion and attenuation of slow P-waves in the background media. Figure 4-3 present the comparison of 1-D seismograms at (1200m, 0m).

We consider the poroelastic modeling as a reference scenario because it can naturally incorporate the FPD effects. Figure 4-2 and Figure 4-3 suggest very good agreement between the S_{PP} amplitude calculated using the PLSM-based and VLSM-based modeling, while the HFLSM-HVLSM-based modeling obviously underestimate the S_{PP} amplitude, and the LFLSM-LVLSM-based modeling overestimate the S_{PP} amplitude. This is to be expected, since the scattering behavior of a fracture is mainly controlled by the stiffness contrast with respect to the background. The HFLSM-HVLSM assumes there is insufficient time for fluid exchange at the fracture interface, the fracture behaves as being sealed and the stiffness of the saturated fracture is

518 maximal, resulting in an underestimated stiffness contrast between fracture and background. The LFLSM-LVLSM assumes
 519 there is enough time for fluid flow between the fracture and background, the deformation of the fracture is maximal, resulting
 520 in an overestimated stiffness contrast with background. However, the VLSM derived from poroelastic theory, however, can
 521 properly incorporate the FPD effects, leading to a frequency-dependent stiffness contrast equivalent to the PLSM. It can be
 522 note that the S_{pp} amplitudes obtained using the LFLSM-LVLSM-based modeling is comparable to that of the PLSM based
 523 modeling, because the FPD effects mainly occur at seismic frequencies closer to the low frequency limit. The S_{pp} travel time
 524 obtained using the four modeling schemes shows good consistency. Figure 2 and Figure 3 also shows that the discrepancy of
 525 the S_{ps} amplitudes is almost negligible. Because the S-wave scattering behavior is mainly controlled by the drained stiffness
 526 contrast between the fracture and the background. The comparison of different modeling schemes demonstrates that the
 527 DLSM-based viscoelastic modeling can appropriately capture the FPD effects on wave scattering of a fluid saturated fracture,
 528 while the two elastic modeling cannot correctly estimate the scattered waves. Figure 1 and Figure 2 demonstrate that the DLSM-
 529 based viscoelastic modeling can appropriately capture the FPD effects on wave scattering of a fluid saturated fracture. However,
 530 the two elastic modeling cannot correctly estimate the S_{pp} amplitudes.



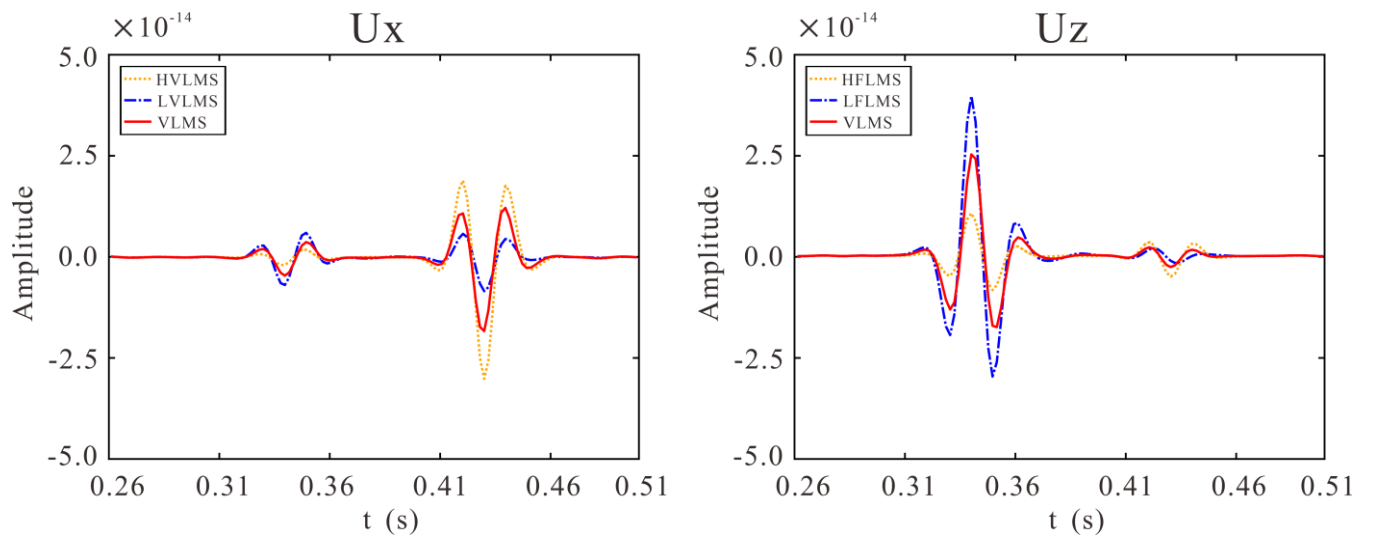


532

533 **Figure 4: Snapshots of the wavefields components U_x and U_z for a single inclined fracture model at 280ms: (a) the PLSM based**

534 **poroelastic modeling, (b) the VLSM based viscoelastic modeling, (c) the LVLSM based elastic modeling and (d) the HVLSM based**

535 **elastic modeling. The blue asterisk and line represent the source and the fracture, respectively.**

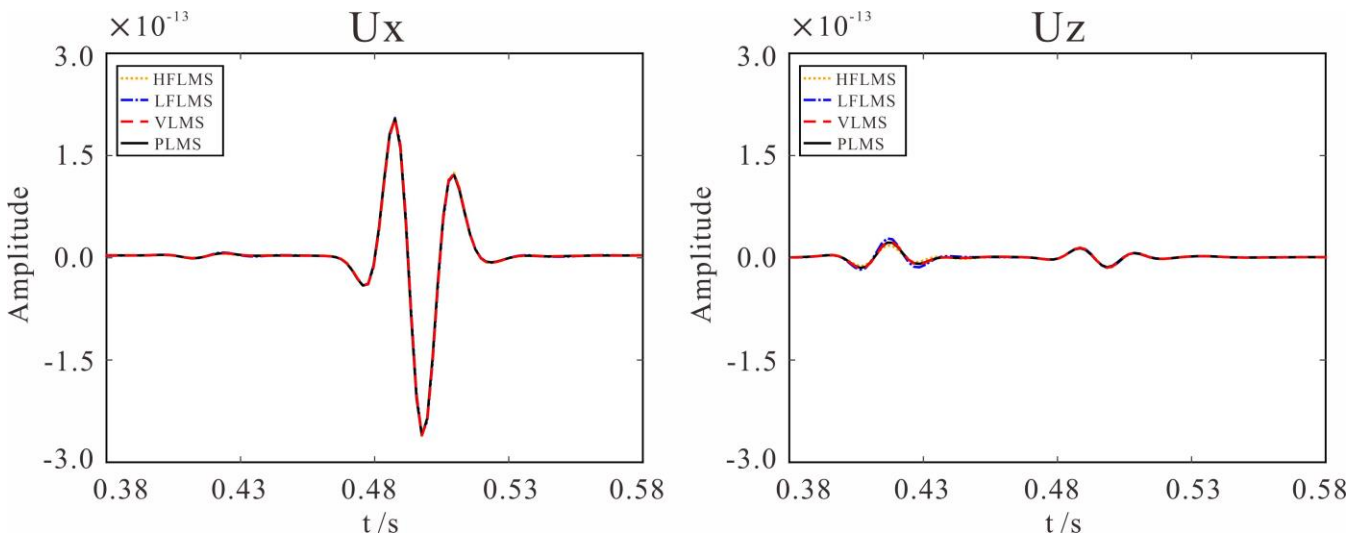


536

537 **Figure 3: Snapshots of the wavefields components U_x and U_z for a single horizontal fracture model at 280ms due to a S-wave point**

538 **source: (a) the PLSM based poroelastic modeling, (b) the VLSM based viscoelastic modeling, (c) the LFLSM based elastic modeling**

539 **and (d) the HFLSM based elastic modeling.**



541 **Figure 5: Comparison of 1-D seismograms components U_x and U_z at (1000m, 0m) for a single inclined fracture model.**

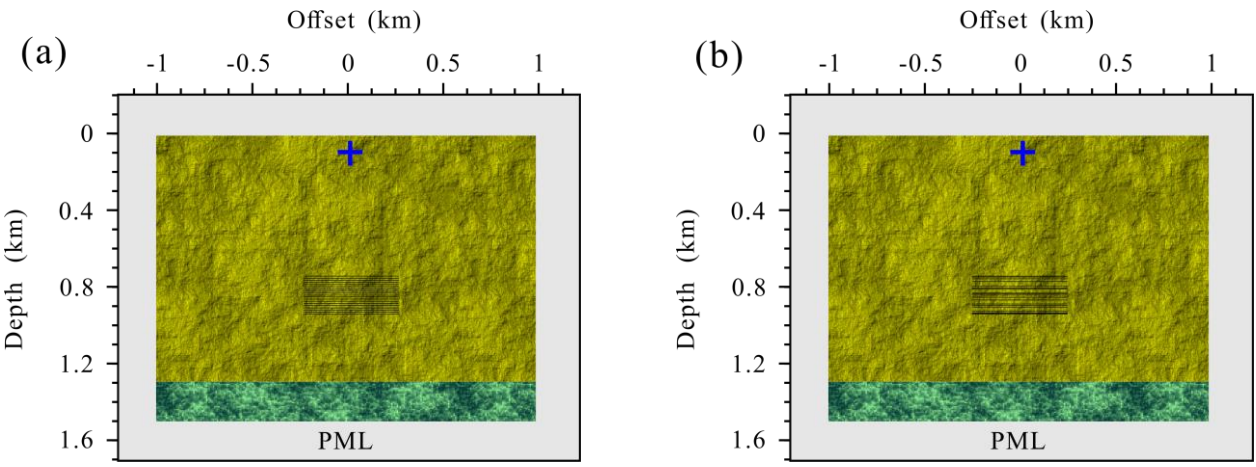
542 **Figure 4: Comparison of 1-D seismograms components U_x and U_z at receiver (1200m, 0m) for a single horizontal fracture model
543 due to a S-wave point source.**

544 The proposed modeling scheme is also applicable to the inclined fracture. Figure 4 shows the 280ms snapshots of the
545 displacement fields for the single inclined fracture model models. Figure 5 is the comparison of 1-D seismograms at
546 (1200m,0m). Figure 4 and Figure 5 show that both the scattered P - and S -waves of a single inclined fracture are strongly
547 affected by the FPD effects.

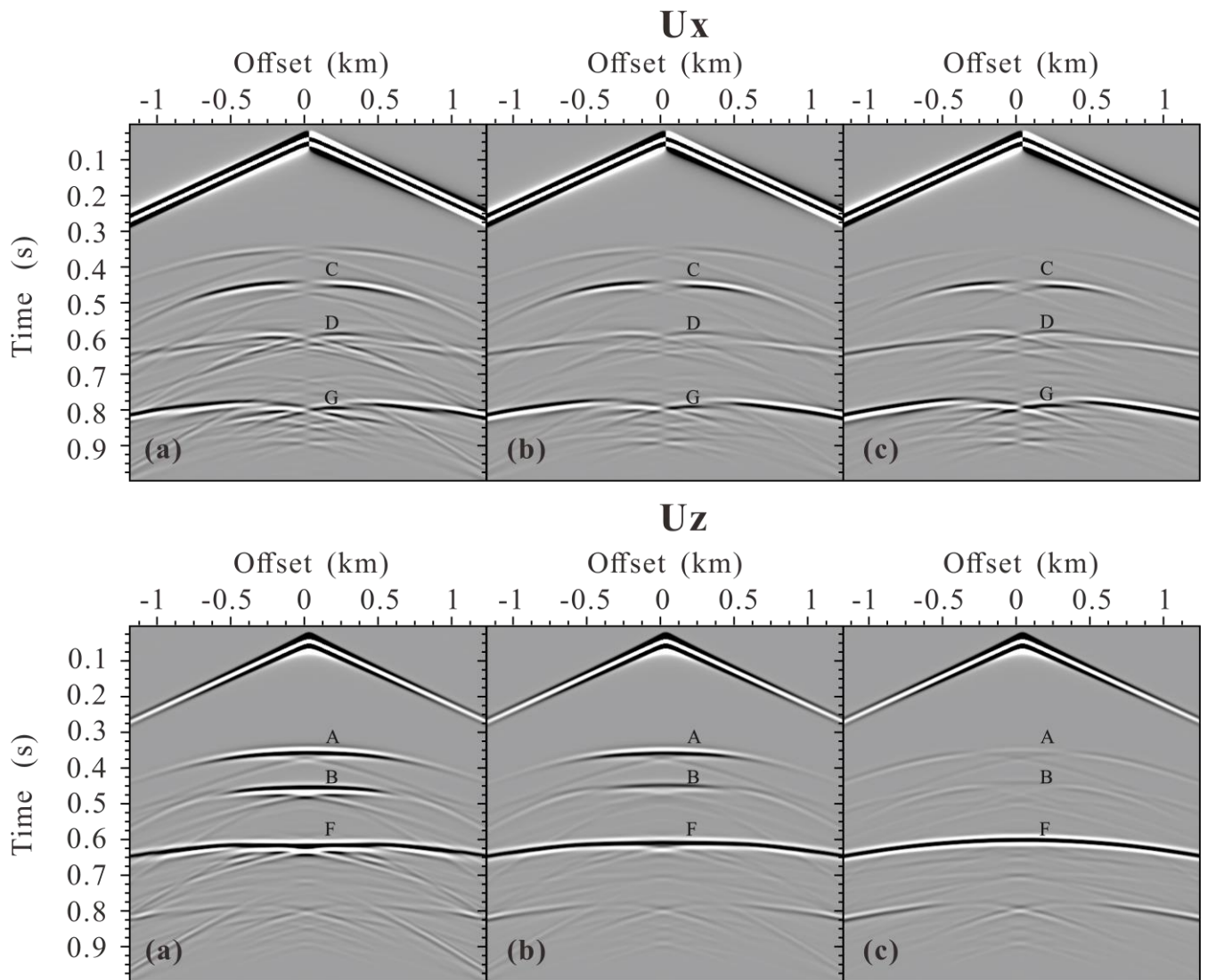
548 **4.2 Fractured reservoir model**

549 **6.2 Fractured reservoir model**

550 In addition to a single fracture, we are more interested in the scattering behavior of discrete distributed fractures system. To
551 this end, we designed two fractured reservoir models containing a set of regularly distributed aligned horizontal fractures and
552 a set of randomly distributed aligned horizontal fractures, respectively, as illustrated in Figure 6. There are 200 horizontal
553 fractures spread over a space of 200m, each extending 500m. The material properties of the fracture, background (yellow
554 region) and underlying (green region) formation are given in Table 1. The model size, grid interval and source location are the
555 same as those in the previous numerical examples. Through a set of aligned horizontal fracture structures is not practical in the
556 actual subsurface, it helps to illustrate the impact of FPD effects on the amplitude and phase of scattered waves of fractures.



557
558 **Figure 6: Schematic diagram of the fractured reservoir model with a set of aligned horizontal fractures: (a)regular distribution**
559 **(b)random distribution. The black segments present the fracture system. The extending of each fracture is 500m.**



560
561 **Figure 7: Seismogram components U_x and U_z of the fractured reservoir model with a set of regularly distributed aligned horizontal**
562 **fractures calculated using (a)the LVLSM, (b)the VLSM, (c)the HVLSM. A, B are scattered P-wave from top and bottom, respectively,**
563 **C and D are scattered converted shear S-wave from top and bottom, respectively, F and G are reflected P-wave and shear converted**
564 **S-wave, respectively.**

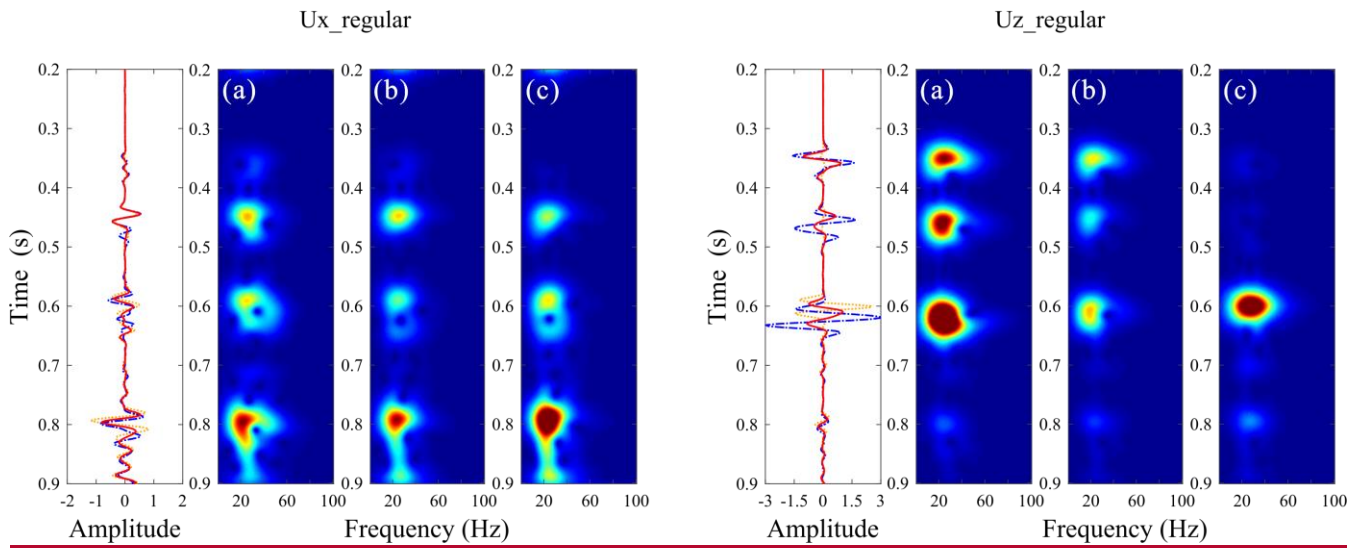
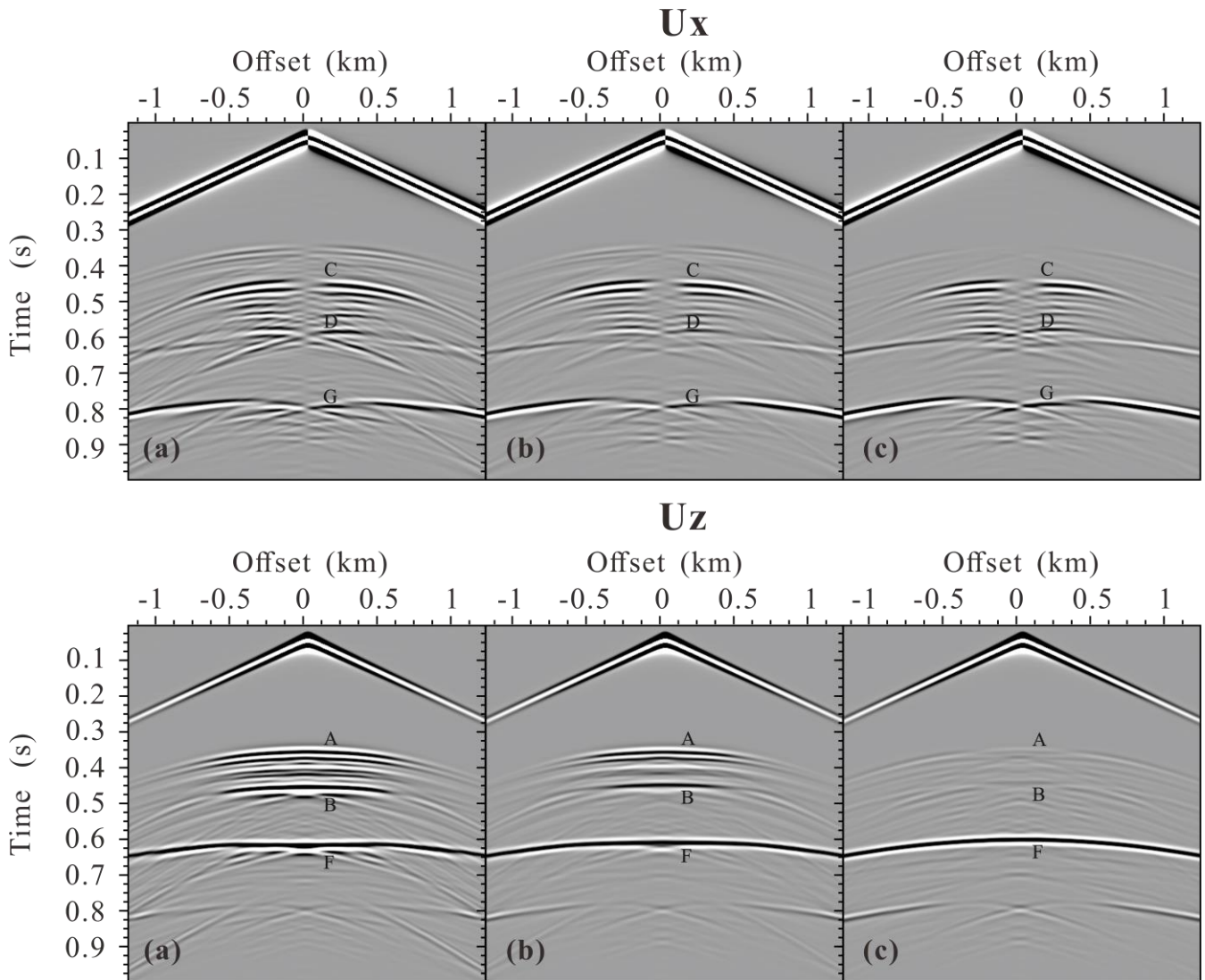


Figure 8: Time-frequency distributions of the middle trace for (b) the LVPLM, (c) the PLSM, and (d) the HVLSM cases in Figure 7.

Figure 7 presents the seismograms of fractured reservoir model with a set of regular distributed aligned horizontal fractures. The scattered compressional wave (S_{PP}) and scattered converted wave (S_{PS}) from the top and bottom of the fractured reservoir, the reflected compressional wave (R_{PP}), converted wave (R_{PS}) from the underlying formation can be clearly identified. Due to the regular distribution of aligned fracture, the fractured reservoir is equivalent to an anisotropic homogeneous media, and therefore the diffracted wave is generated only at the edges of the fractured reservoir. Similar to the single fracture case, the amplitude of the S_{PP} from the top and bottom of the fractured reservoir obtained by the HVLSM-based modeling is weakest (underestimated), that obtained by LVLSM-based modeling is strongest (overestimated), and that obtained by the VLSM-based modeling is intermediate. We notice that the S_{PP} amplitudes from the bottom of the fractured reservoir obtained by the LVLSM-based and HVLSM-based modeling are slightly smaller than those from the top, while the S_{PP} amplitude from the bottom obtained by the VLSM-based modeling is much smaller than that from the top. This is expected, since the VLSM-based modeling scheme can capture the wave attenuation and dispersion due to the FDP effects between the fracture system and background, while the LVLSM and HVLSM represent non-attenuated and non-dispersive elastic processes. Another evidence for attenuation is that the R_{PP} amplitudes of underlying formation calculated by the HVLSM-based and LVLSM-based modeling are almost equal, while the R_{PP} amplitude calculated by the VLSM-based modeling is much smaller. Figure 7 also shows that the arrival times of S_{PP} from the bottom and R_{PP} from underlying formation obtained by the three modeling schemes are different.

To show the trend of frequency-dependent attenuation and dispersion, time-frequency distribution of the middle trace was computed for three modeling schemes. Figure 8 clearly shows that the frequency content and energy of the scattered and reflected waves calculated by VLSM tend to decrease strongly, while the frequency content and energy calculated by HVLSM and LVLSM remain steady. The impact of FPD effects on the S_{PS} and R_{PS} is similar to that of the S_{PP} and R_{PP} , but to a much weaker extent.

589 In addition to regularly distributed fractures, our proposed modeling scheme can also simulate the wave scattering of random
 590 distributed fractures. Figure 9 presents the seismograms of fractured reservoir model with a set of random distributed aligned
 591 horizontal fractures. Figure 10 presents the time-frequency distributions of the middle trace for three modeling schemes cases
 592 in Figure 9. Due to the random distribution of aligned fracture, the fractured reservoir exhibits a stronger heterogeneity,
 593 resulting in more prevalent diffracted wave (coda wave) in Figure 9 than in Figure 7. Except for the diffracted wave, the
 594 scattered and reflected waves in the random distribution case is similar to those in the regular distribution case due to the FPD
 595 effect. The two fractured reservoir models suggest that the scattered waves from the bottom of the fractured reservoir are
 596 attenuated and dispersed by the FPD effects and the reflected waves can retain the relevant attenuation and dispersion
 597 information.



599 **Figure 9: Seismogram components U_x and U_z of the fractured reservoir model with a set of randomly distributed aligned horizontal
 600 fractures calculated using (a) the LVLSM, (b) the VLSM, (c) the HVLSM. A, B are scattered P-wave from top and bottom,
 601 respectively, C and D are scattered converted shear S-wave from top and bottom, respectively, F and G are reflected P-wave and
 602 shear converted S-wave, respectively.**

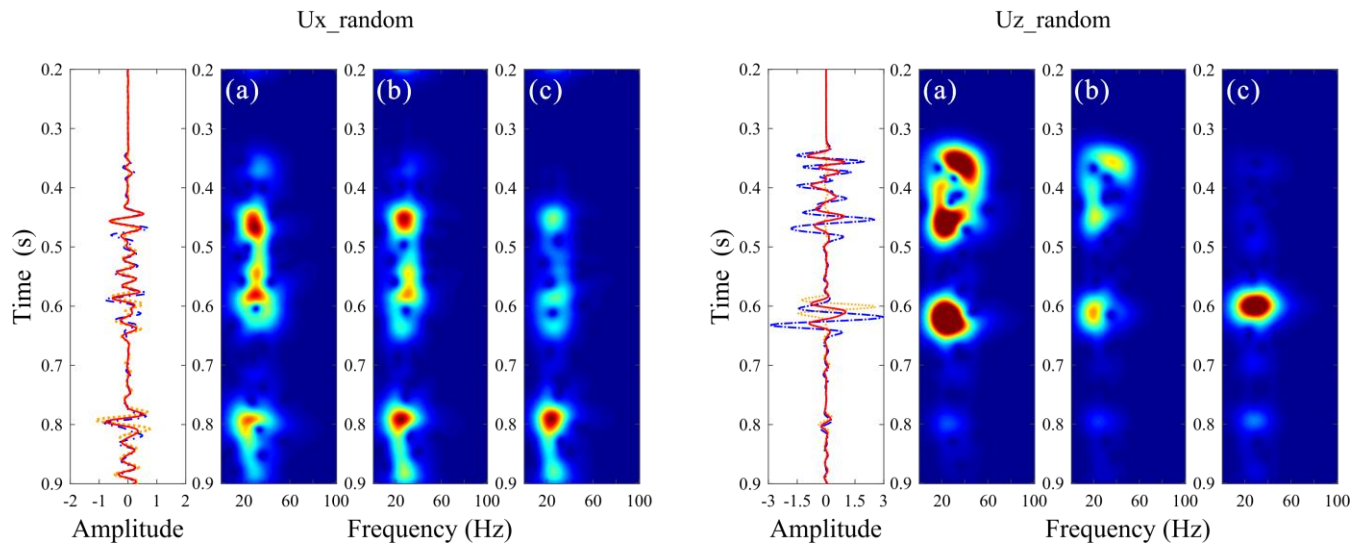


Figure 10: Time-frequency distributions of the middle trace for (b) the LVPLM, (c) the PLSM, and (d) the HVLSM cases in Figure 9.

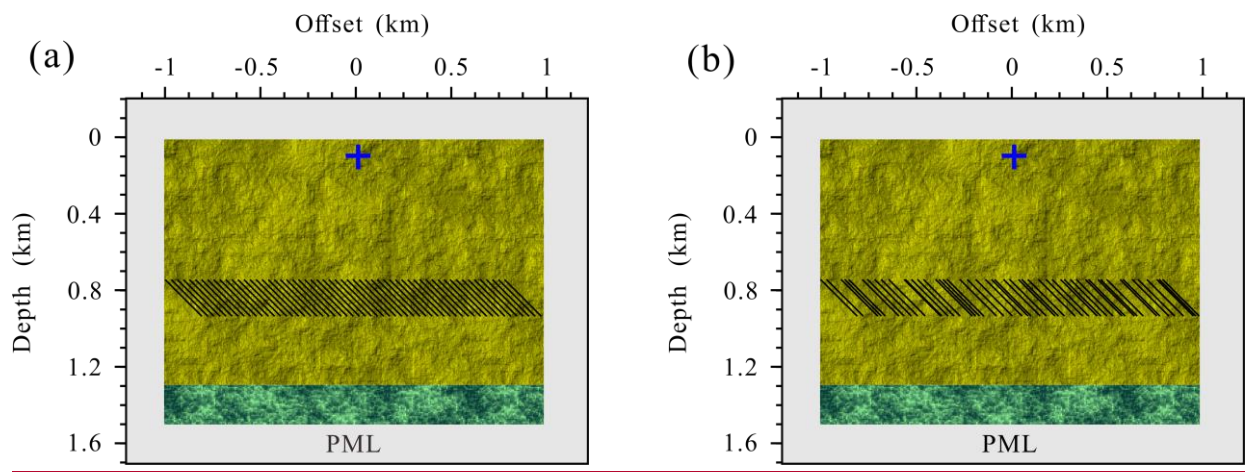
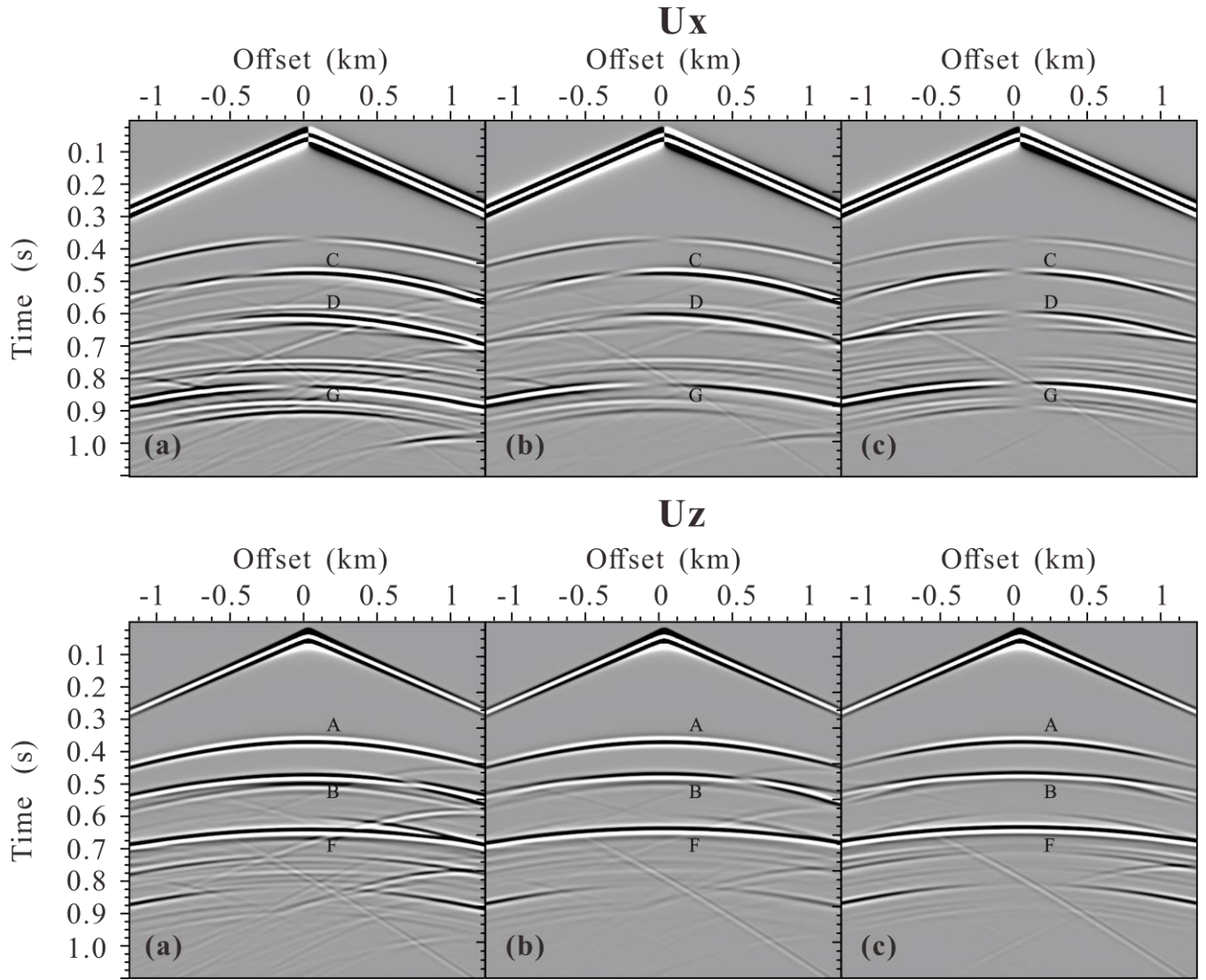
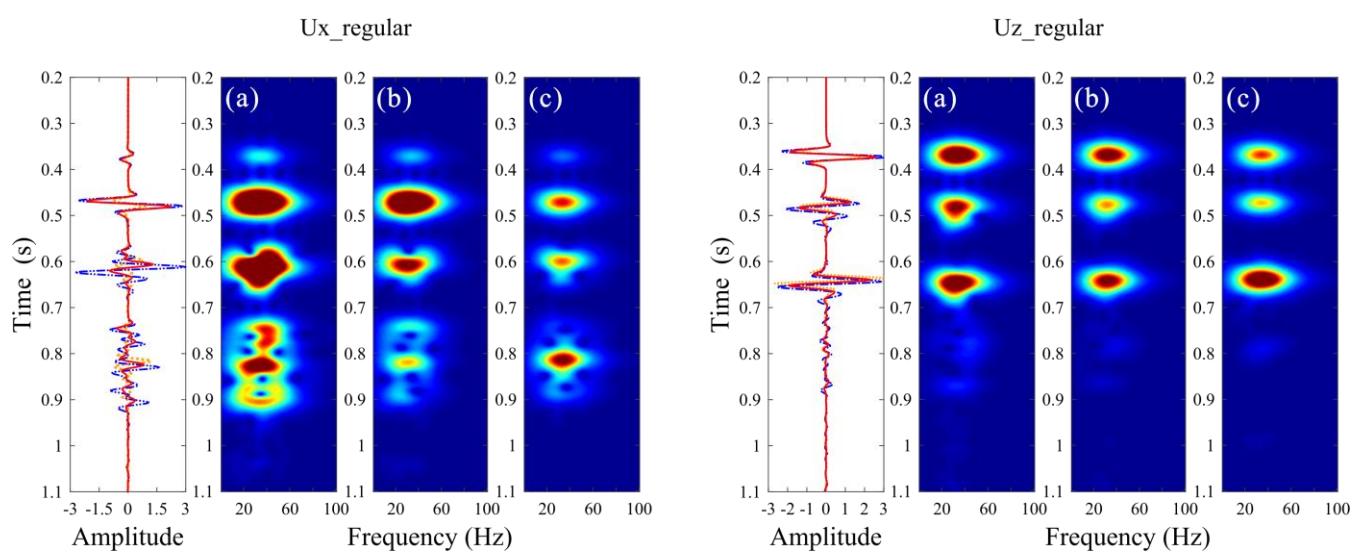


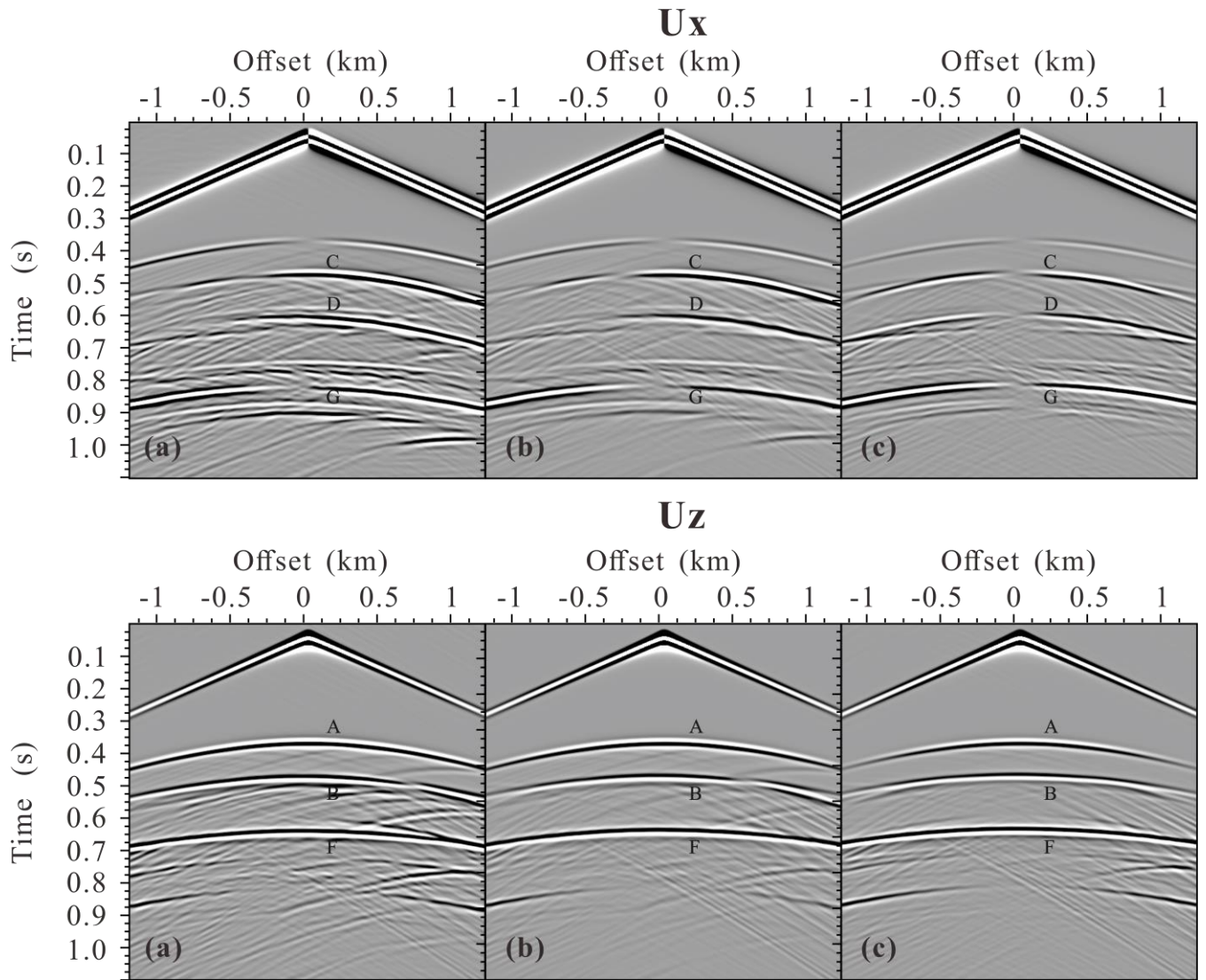
Figure 11: Schematic diagram of the fractured reservoir model with a set of aligned inclined fractures: (a)regular distribution (b)random distribution. The black segments present the fracture system. The extending of each fracture is 282.8m.



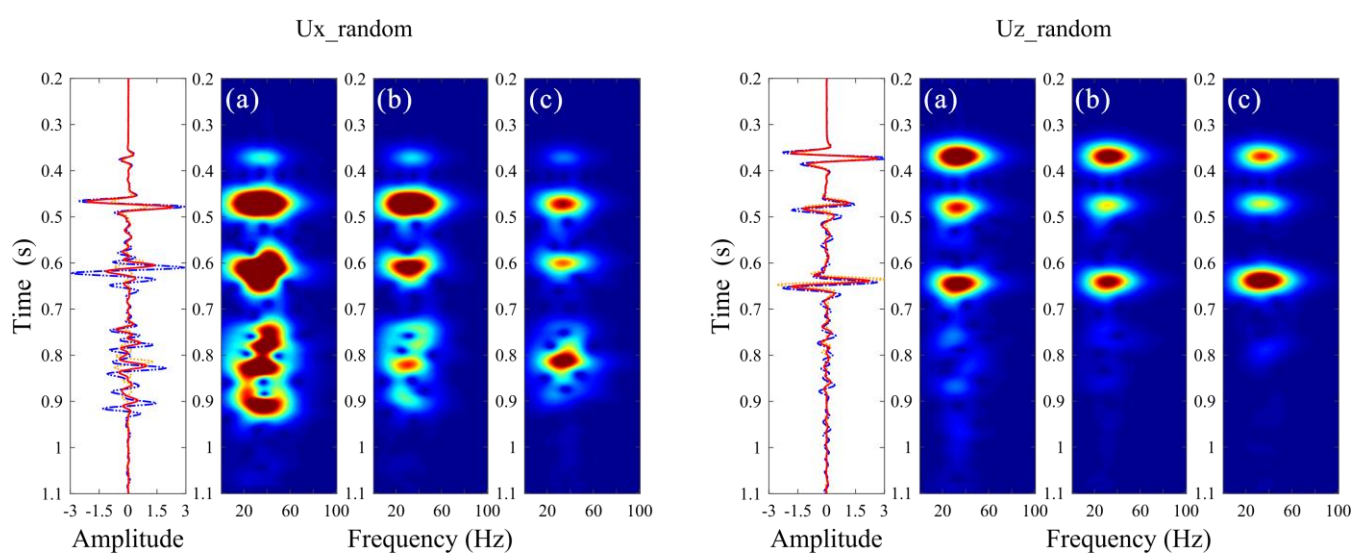
610 **Figure 12: Seismogram components U_x and U_z of the fractured reservoir model with a set of regularly distributed aligned inclined**
611 **fractures calculated using (a) the LVLSM, (b) the VLSM, (c) the HVLSM. A, B are scattered P -wave from top and bottom,**
612 **respectively, C and D are scattered converted shear S -wave from top and bottom, respectively, F and G are reflected P -wave and**
613 **shear converted S -wave, respectively.**



615 **Figure 13: Time-frequency distributions of the middle trace for (b) the LVPLM, (c) the PLSM, and (d) the HVLSM cases in Figure**
616 **12.**



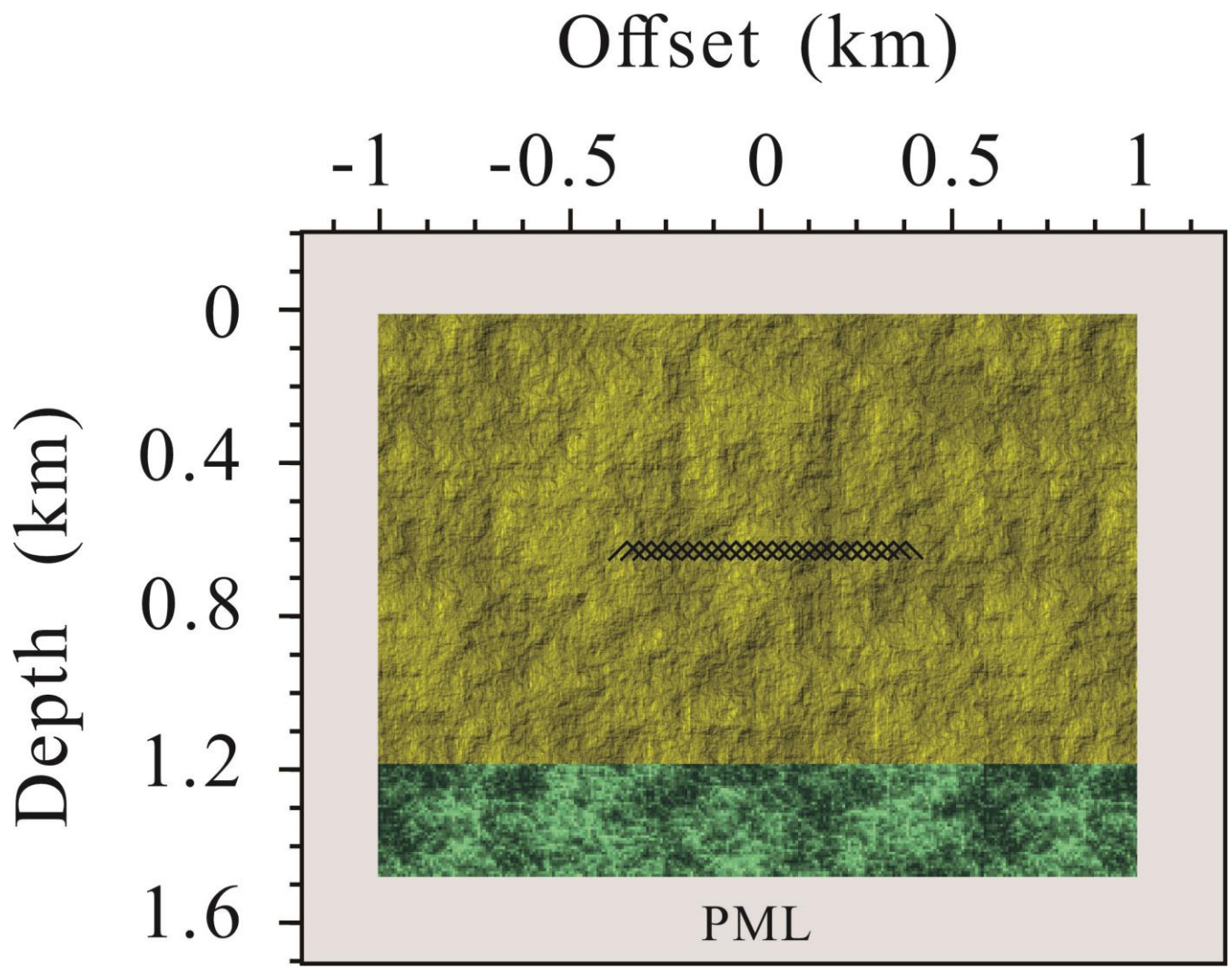
617
618 **Figure 14: Seismogram components U_x and U_z of the fractured reservoir model with a set of randomly distributed aligned inclined**
619 **fractures calculated using (a) the LVLSM, (b) the VLSM, (c) the HVLSM. A, B are scattered P -wave from top and bottom,**
620 **respectively, C and D are scattered converted shear S -wave from top and bottom, respectively, F and G are reflected P -wave and**
621 **shear converted S -wave, respectively.**



622
623 **Figure 15: Time-frequency distributions of the middle trace for (b) the LVPLM, (c) the PLSM, and (d) the HVLSM cases in Figure**
624 **14.**

625 To validate the effectiveness of our proposed modeling scheme in a more practical underground fractured reservoir, we replace
626 a set of aligned horizontal fractures in the original model with a set of aligned inclined fractures, as illustrated in Figure 11.
627 Figure 12 and presents the seismograms of fractured reservoir model with a set of regular distributed aligned inclined fractures
628 and Figure 13 shows the time-frequency distributions of the middle trace for three modeling schemes. Figure 14 and Figure
629 15 present the seismograms of fractured reservoir model with a set of random distributed aligned inclined fractures and the
630 time-frequency distributions of the middle trace for three modeling schemes, respectively. All results of PLSM-based modeling
631 capture the influence of FPD effects on the amplitude and phase of scattered waves, validating the effectiveness of our proposed
632 modeling scheme. Figure 12 and Figure 14 also show the different scattering characteristics of the randomly and regularly
633 distributed incline fractures: many coda waves are generated by the randomly distributed fractures due to a stronger
634 heterogeneity.

635 In addition to a single fracture, we are more interested in the scattering behavior of discretely distributed fractures system. To
636 this end, we designed a fractured reservoir model containing a conjugate fracture system (consisting of two sets of mutually
637 perpendicular fractures, as illustrated in Figure 5). The normal spacing and extending of this set of conjugate fractures are
638 1.768m and 70.7m, respectively. The material properties of the fracture, background (yellow region) and underlying (green
639 region) formation are given in Table 1. The model size, grid interval and source location are the same as those in the previous
640 numerical examples.



641
642 **Figure 5: Schematic diagram of the fractured reservoir model I with a conjugate fracture system. The black segments present the**
643 **fracture system. The normal spacing and extending of each fracture are 1.768m and 70.7m, respectively.**

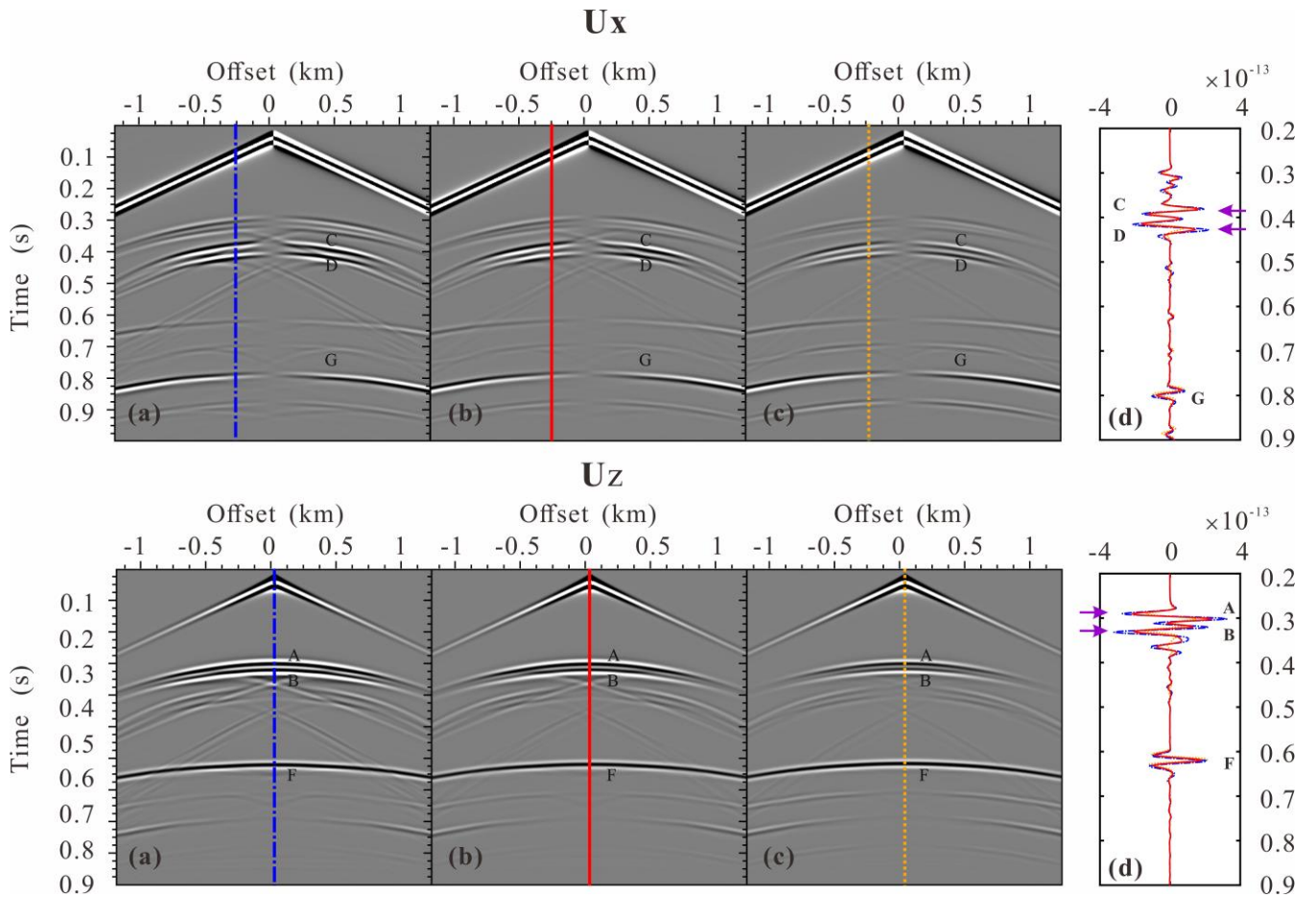
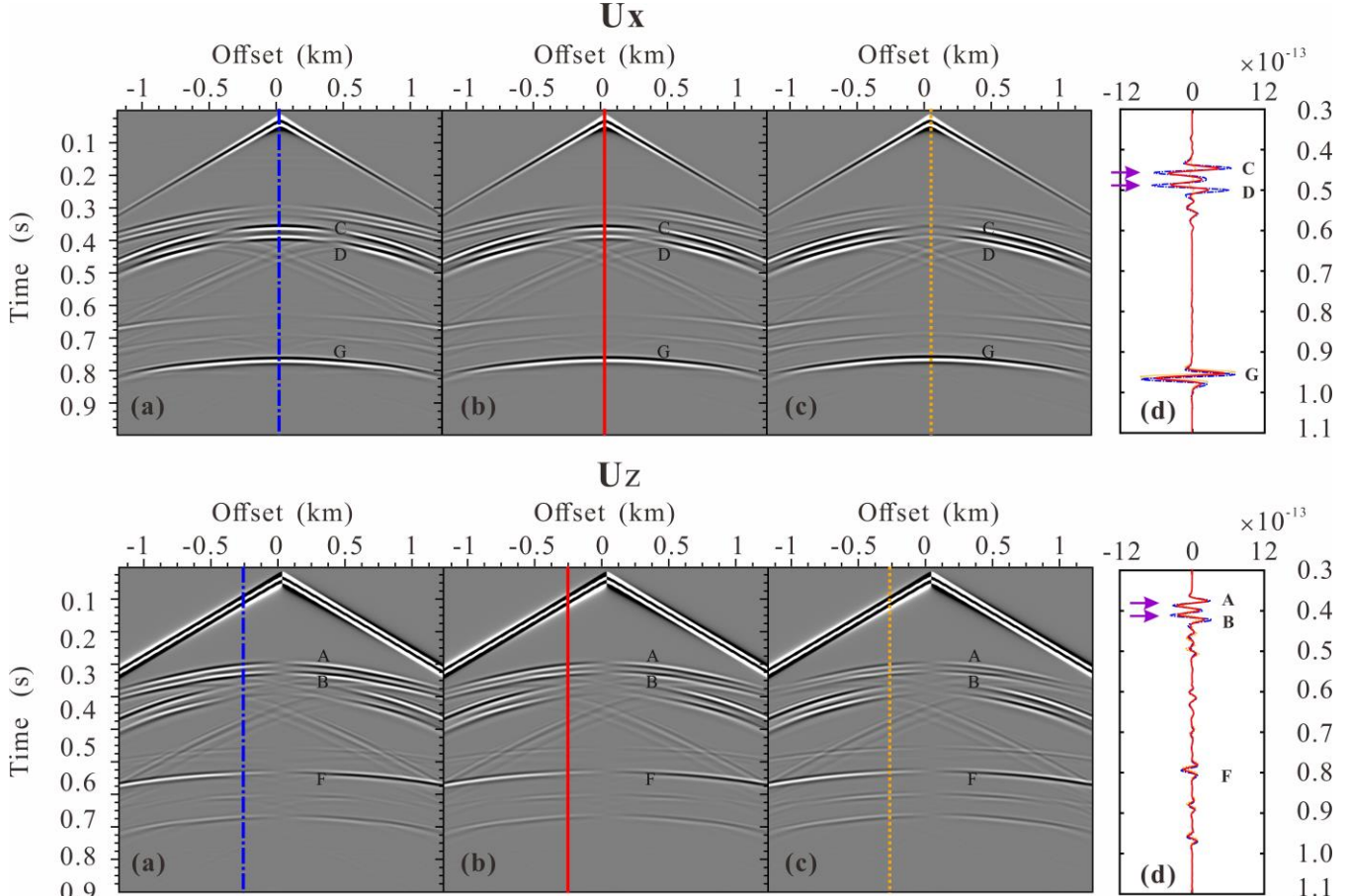


Figure 6: Seismogram components U_x and U_z of the fractured reservoir model I due to a P-wave point source: calculated using (a) the LFLSM, (b) the VLSM, (c) the HFLSM. (d) is the comparison of single trace extracted from the three gathers. A and B are scattered compressional wave from top and bottom, respectively, C and D are scattered converted wave top and bottom, respectively, F and G are reflected compressional wave and converted wave, respectively, E is scattered diffracted wave.

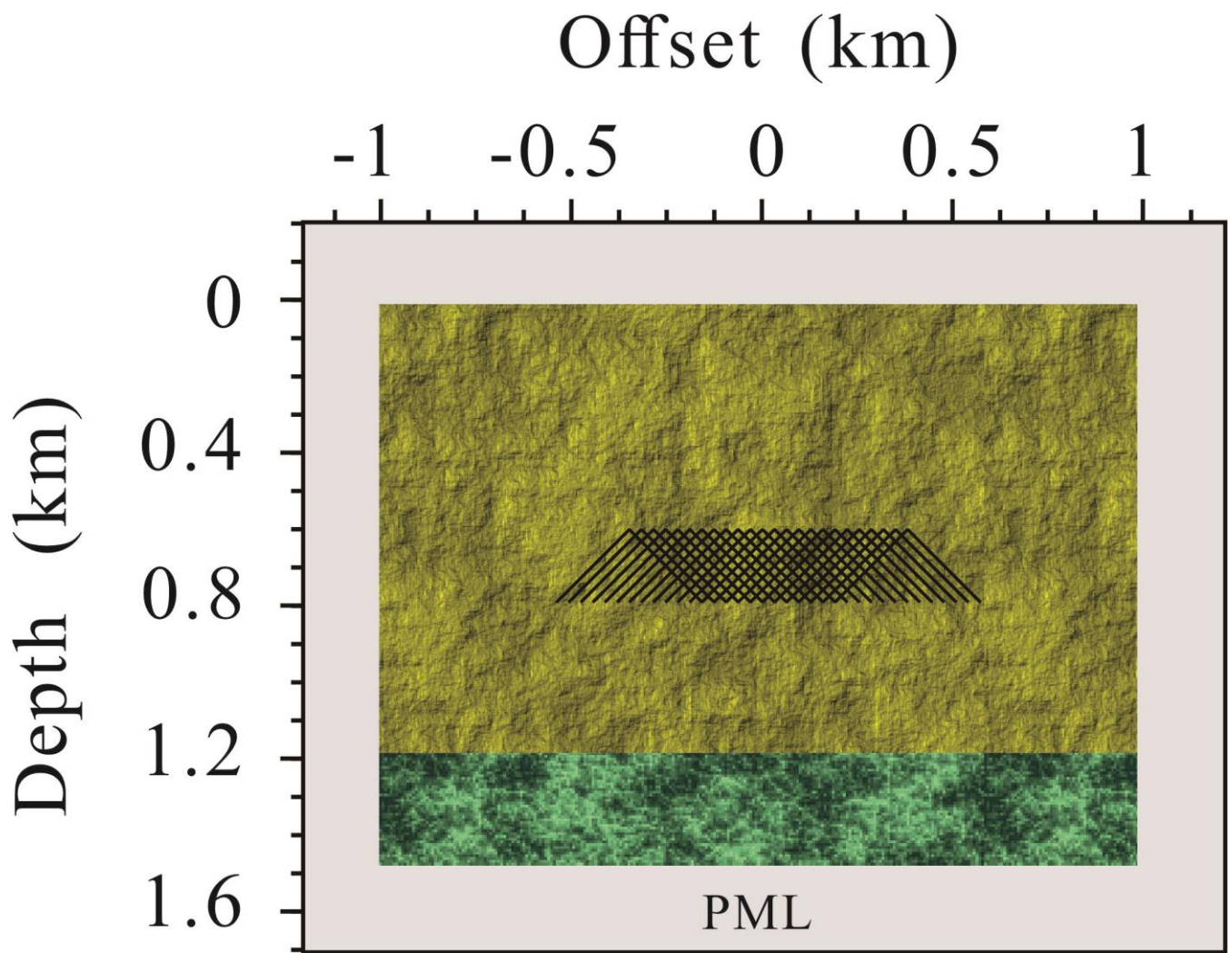
Figure 6 presents the seismograms of fractured reservoir model I for a P-wave point source. The scattered compressional wave (S_{pp}) and scattered converted wave (S_{ps}) from the top and bottom of the fractured reservoir, the reflected compressional wave (R_{pp}), converted wave (R_{ps}) from the underlying formation, diffracted wave at the edge of the fractured reservoir can be clearly identified. Similar to the single fracture case, the amplitude of the S_{pp} from the top of the fractured reservoir obtained by the HFLSM based modeling is weakest (underestimated), that obtained by LFLSM based modeling is strongest (overestimated), and that obtained by the VLSM based modeling is intermediate (accurate). The purple arrows in the Figure 6 (d) indicate that the S_{pp} from the bottom of the fractured reservoir obtained by the LFLSM based and HFLSM based modeling has a slightly larger amplitude than that from the top, while the S_{pp} from the bottom of the fractured reservoir obtained by the VLSM based modeling has a slightly smaller amplitude than that from the top. This is expected, since the VLSM based modeling scheme can capture the wave attenuation and dispersion due to the FDP effects between the fracture system and background, while the LFLSM and HFLSM represent non-attenuated and non-dispersive elastic processes. However, due to the weak degree of dispersion, the S_{pp} travel time obtained by the three modeling schemes is almost consistent. Figure 6 shows that the amplitudes of the R_{pp} from the underlying formation calculated by the HFLSM based and LFLSM based modeling are almost equal, while

663 that calculated by the VLSM based modeling is attenuated and dispersed. That again indicates the VLSM based modeling can
 664 capture the FPD effects. The S_{ps} and R_{ps} show similar behavior as the S_{pp} and R_{pp} . Figure 6 suggests that the scattered waves
 665 from the bottom of the fractured reservoir are attenuated and dispersed by the FPD effects and the reflected waves can retain
 666 the relevant attenuation and dispersion information.



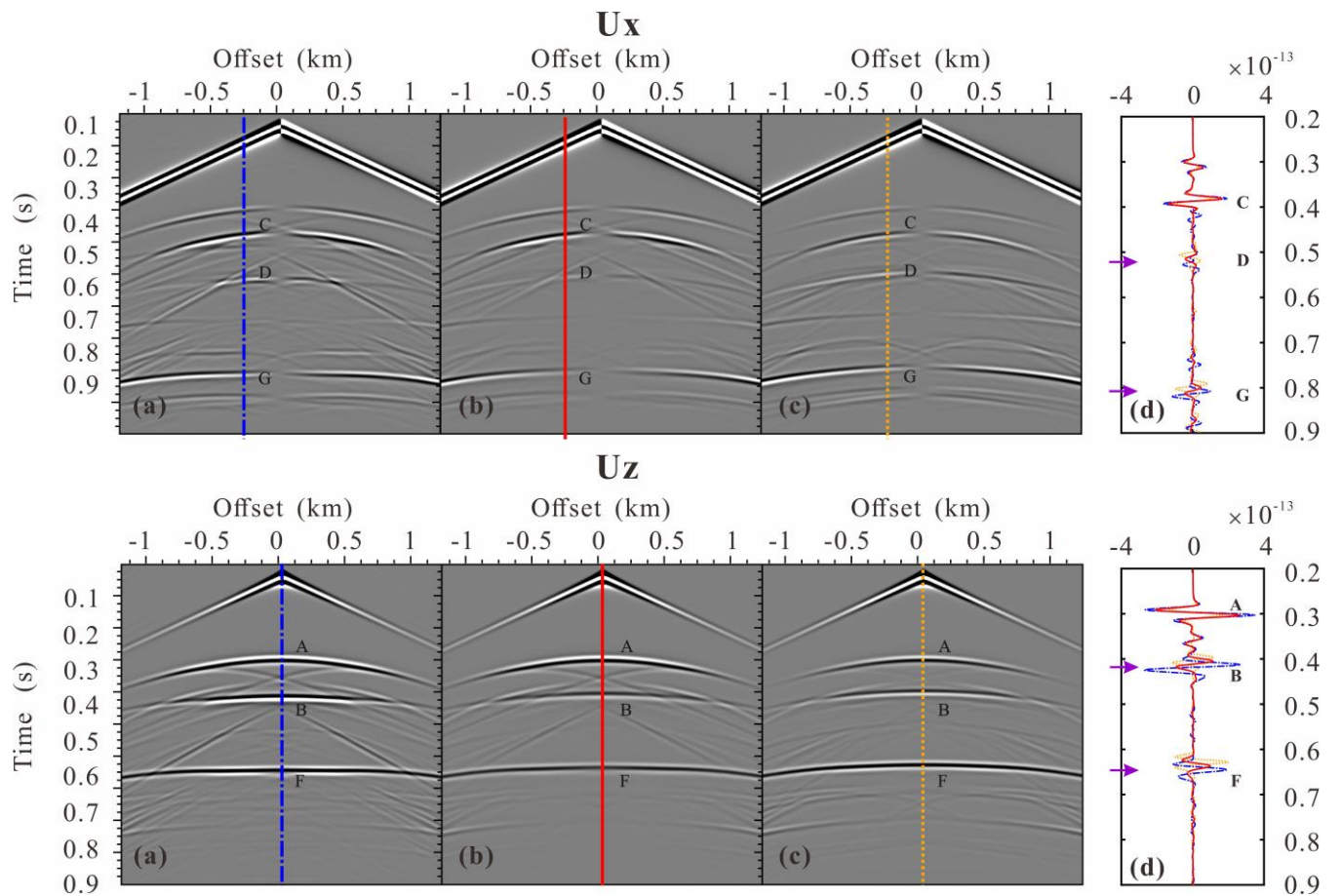
667
 668 **Figure 7: Seismogram components U_x and U_z of the fractured reservoir model I due to a S-wave point source: calculated using (a)**
 669 **the LFLSM, (b) the VLSM, (c) the HFLSM. (d) is the comparison of single trace extracted from the three gathers. A, B are scattered**
 670 **converted SP wave from top and bottom, respectively, C and D are scattered shear SS wave from top and bottom, respectively, F**
 671 **and G are reflected converted SP wave and shear SS wave, respectively, E is scattered diffracted wave.**

673 Figure 7 presents the seismograms of fractured reservoir model I for a S-wave point source. The scattered converted wave (S_{sp})
 674 and shearing wave (S_{ss}) from the top and bottom of the fractured reservoir, the reflected converted wave (R_{sp}) and shearing
 675 wave (R_{ss}) from the underlying formation can be identified in Figure 7. Unlike the case of single horizontal fracture, the FPD
 676 effects between a conjugate fracture system and background can attenuate and disperse the S_{pp} , S_{ps} , R_{pp} and R_{ps} for a S-wave
 677 point source exploration survey.

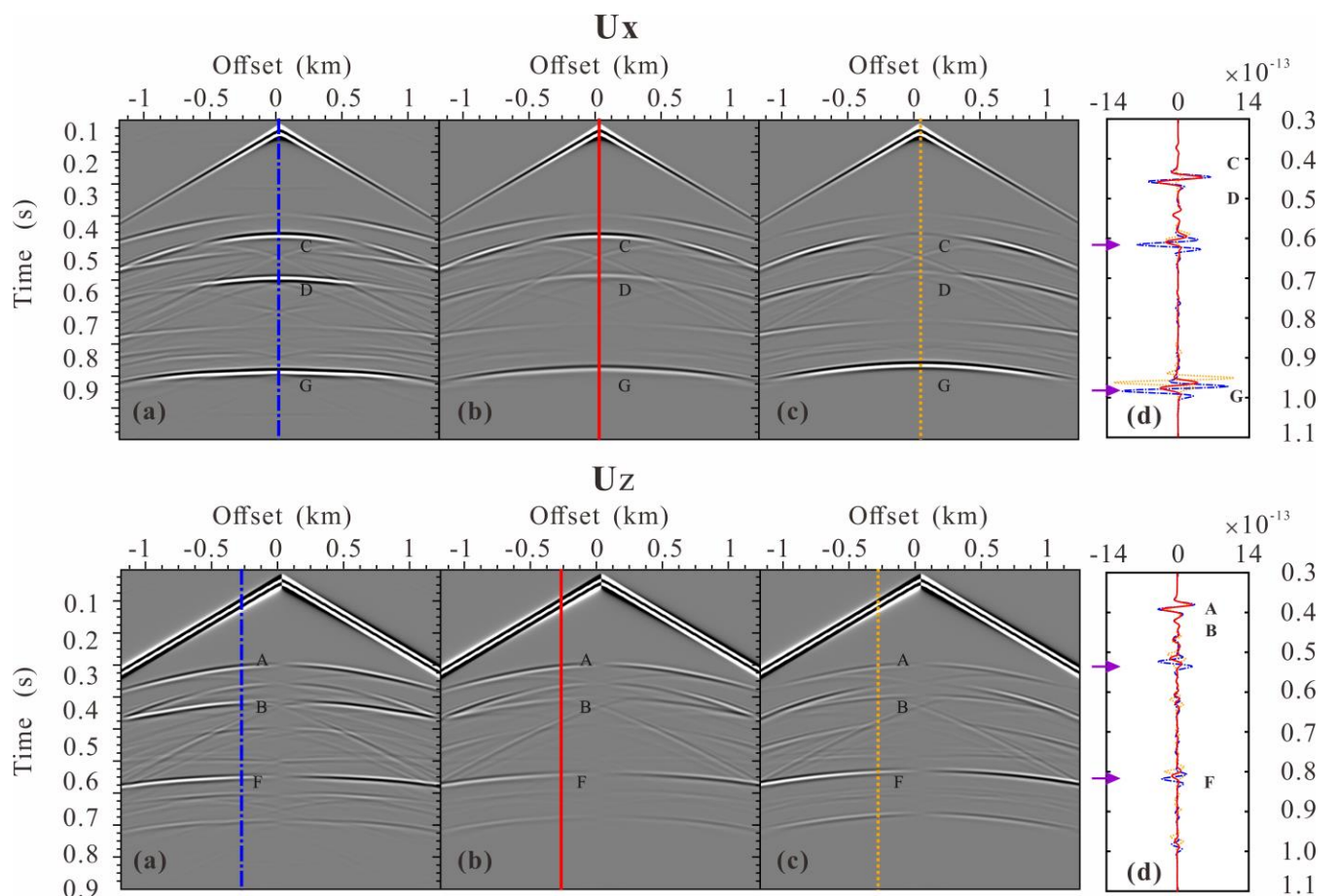


678
679 **Figure 8: Schematic diagram of the fractured reservoir model II. The normal spacing and extending of each fracture are 1.768m**
680 **and 282.8m, respectively.**

681 The attenuation and dispersion caused by FDP effects are strongly affected by the thickness of the reservoir. In general, the
682 thicker the fractured reservoir, the more severe attenuation and dispersion of the seismic wave. To demonstrate the strong
683 attenuation and dispersion caused by FDP effect, we modify the fractured model I, increase each fracture to 282.8m without
684 changing other parameters, and obtain a fractured model II. Figure 9 presents the seismograms of fractured reservoir model II
685 for a P wave point source. Figure 9 shows that the S_{pp} and S_{ps} from the bottom of the fractured reservoir and the R_{pp} and R_{ps}
686 from the underlying formation obtained by the VLSM based modeling are strongly attenuated and dispersed, proving that the
687 VLSM based modeling can be captured the FPD effects when seismic waves travel through the fractured reservoir. Figure 10
688 presents the seismograms of the fractured reservoir model II for a S wave point source. Figure 10 shows that the scattered and
689 reflected waves obtained by VLSM based modeling are also strongly attenuated and dispersed.



690
691 **Figure 9: Seismogram components U_x and U_z of the fractured reservoir model II due to a P-wave point source: calculated using (a)**
692 **the LFLSM, (b) the VLSM, (c) the HFLSM. (d) is the comparison of single trace extracted from the three gathers. The meanings of**
693 **A, B, C, D, E, F and G are same as those in Figure 9.**

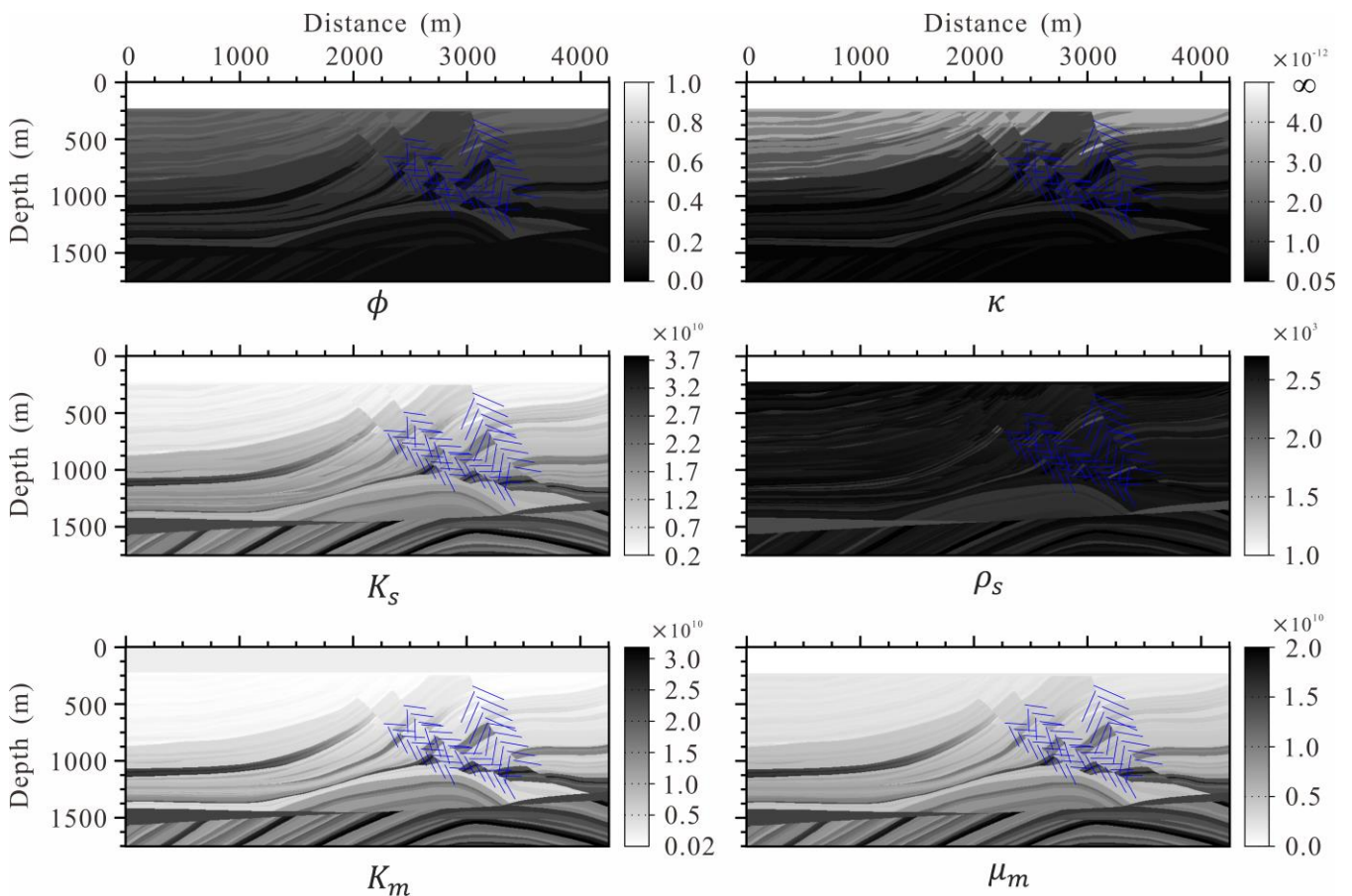


695 **Figure 10: Seismogram components U_x and U_z of the fractured reservoir model I due to a S-wave point source: calculated using (a)**
 696 **the LFLSM, (b) the VLSM, (c) the HFLSM. (d) is the comparison of single trace extracted from the three gathers. The meanings of**
 697 **A, B, C, D, E, F and G are same as those in Figure 10.**

698 4.3 Modified Marmousi model

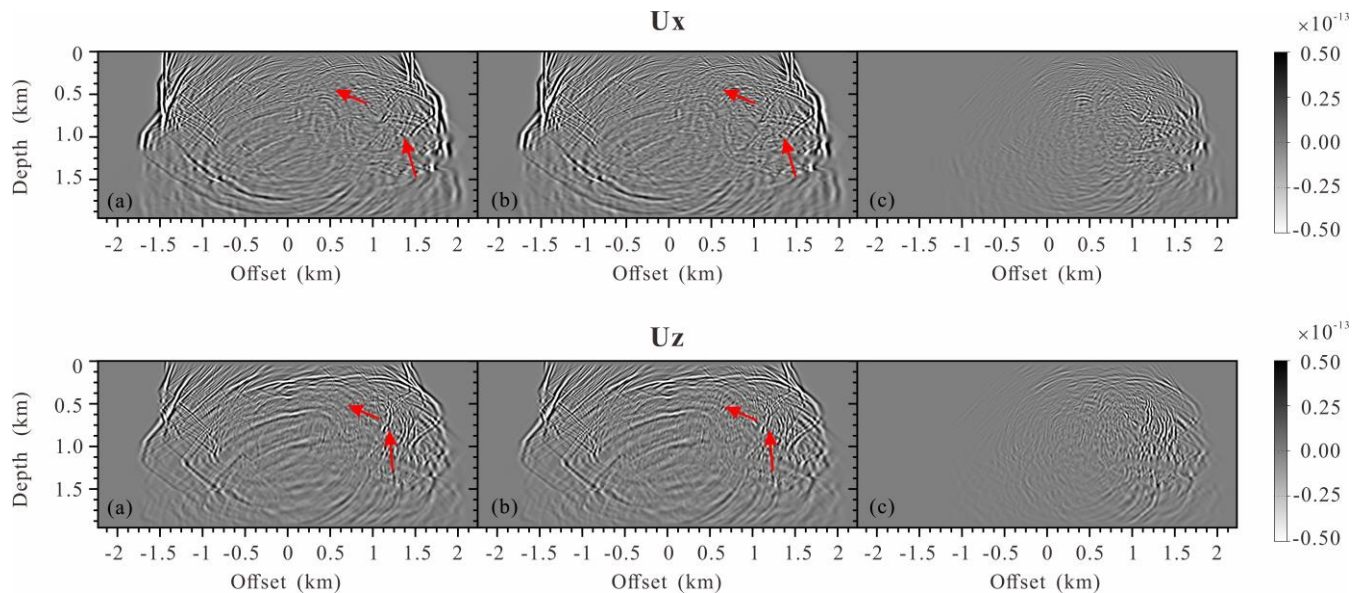
699 6.3 Modified Marmousi model

700 We test the proposed VLSM-based modeling scheme on a more complex modified Marmousi model. To modify the Marmousi
 701 model, we generate a porosity model, permeability model and discrete large-scale fracture system, and transform the original
 702 P-wave velocity and density into the fluid saturated bulk and shear modulus of the background by a constant Poisson's ratio
 703 0.5, and finally obtain the grain bulk modulus, the frame bulk and shear modulus of the background through Gassmann
 704 equation and empirical formula $K_m = (1 - \phi)^{\frac{3}{(1-\phi)}} K_s$. The input physical properties and elastic modulus models of the modified
 705 Marmousi model are present in Figure 11. The fluid density, bulk modulus and viscosity are the same as in Table 1. The model
 706 size is 4250m \times 1750m with grid interval 5m and a 100m thick PML boundary. The source is located at the surface (2125m,
 707 0m). A Ricker wavelet with a central frequency of 25Hz is used as the temporal source excitation.

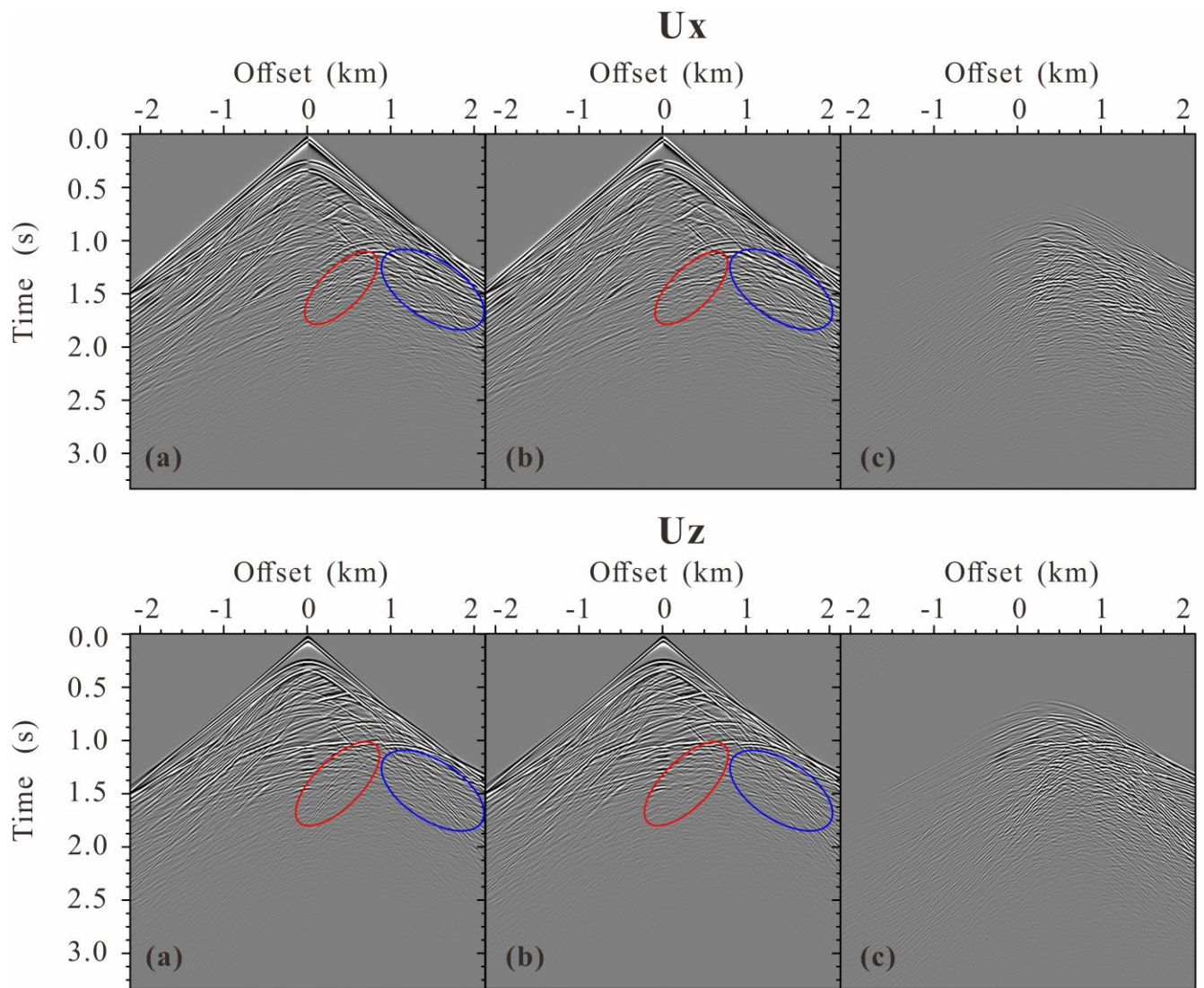


708 **Figure 11: The physical properties and elastic modulus models of the modified Marmousi model.**

709



710
 711 **Figure 1217:** Snapshots of the wavefields components U_x and U_z at 1000ms: (a) the original Marmousi model without fractures,
 712 (b) the modified Marmousi model with fractures and (c) the differences.



713
 714 **Figure 1218:** Seismogram components U_x and U_z : (a) the modified Marmousi model with fractures, (b) the original Marmousi model
 715 without fractures and (c) the differences.

716 Figures 12-17 shows the snapshots of displacement fields at 1000ms. The figure clearly shows the scattered P- and S-waves

717 by the discrete distributed large-scale fractures. The results with such a complex model clearly verify the numerical
718 implementation and the code. We also calculate the seismograms of the displacement shown in Figure 1318. The seismograms
719 obtained by our proposed modeling scheme present the scattered seismic waves by the discrete fractures.

720 **7. 5 Conclusions**

721 In this work, we have developed a numerical modeling scheme including FPD effects for discrete distributed large-scale
722 fractures embedded in fluid saturated porous rock. To capture the FPD effects between the fractures and background, the
723 fractures are represented as Barbosa's VLSM with complex-valued and frequency-dependent fracture compliances. Using
724 Coates and Schoenberg's local effective medium theory and Barbosa's VLSM, we derive the effective anisotropic viscoelastic
725 compliances in each spatial discretized cell by superimposing the compliances of the background and the fractures. The
726 effective governing equations of each numerical cells are expressed by the derived effective compliances and discretized by
727 mixed-grid stencil FDFD. The proposed modeling scheme can be used to study the impact of mechanical and hydraulic of
728 fracture properties on seismic scattering. The main advantage of our proposed modeling scheme over poroelastic modeling
729 schemes is that the fractured domain can be modeled using a viscoelastic solid, while the rest of the domain can be modeled
730 using an elastic solid.

731 The scattered P-wave of a fluid saturated horizontal fracture calculated by VLSM-based modeling is strongly affected by the
732 FPD effects, while the scattered S-wave is less sensitive, which is consistent the result of PLSM-based modeling. However,
733 the LVLSM-based modeling overestimates the scattered P-wave and the HVLSM-based modeling underestimates the scattered
734 P-wave. The numerical results valid that the proposed VLSM-based modeling can include the FPD effects and thus accurately
735 estimate the scattered wave of the horizontal fracture. The results of the fractured reservoir models show that the amplitudes
736 of the scattered waves from the top of the fractured reservoir are affected by the fluid stiffening effects due to the FPD effects.
737 The scattered waves from the bottom of the fractured reservoir are also attenuated and dispersed by the FPD effects in addition
738 to the fluid stiffening effects and the reflected waves can retain the relevant attenuation and dispersion information. Randomly
739 distributed fractures can also result in a different scattering characteristic than regularly distributed fractures, i.e. a large number
740 of coda waves are generated due to increased inhomogeneity. The results of the modified Marmousi model clearly show the
741 scattered waves by the discrete distributed large-scale fractures and verify the proposed numerical modeling scheme. The
742 numerical results of the single horizontal fracture model with a P point source valid that the proposed VLSM-based modeling
743 can include the FPD effects and thus accurately estimate the scattered wave of the horizontal fracture. In contrast, the LFSLM-
744 based modeling overestimates the scattered wave and the HFSLM-based modeling underestimates the scattered wave. The
745 numerical results with an S point source show that the scattered waves off a single horizontal fracture is less sensitive to FDP
746 effects. Due to the differences in fracture orientation, the results of the conjugate fractured reservoir model are quite different

747 from those of the single horizontal fracture model. For both P and S point sources, the amplitudes of the scattered waves from
 748 the top of the fractured reservoir are affected by the fluid stiffening effects due to the FPD effects. The scattered waves from
 749 the bottom of the fractured reservoir are also attenuated and dispersed by the FPD effects in addition to the fluid stiffening
 750 effects and the reflected waves can retain the relevant attenuation and dispersion information. The results of the modified
 751 Marmousi model clearly show the scattered P and S waves by the discrete distributed large scale fractures and verify the
 752 proposed numerical modeling scheme. The proposed numerical modeling scheme is expected not only to improve the
 753 estimations of seismic wave scattering from discrete distributed large-scale fractures but can also to improve migration quality
 754 and the estimation of fracture mechanical characteristics in inversion.

755 Appendix A: The coefficients related to spatial derivative operators

756 We define coefficient vectors \mathbf{T}_k ($k = 1, 2, 3, 4$) and the derivative operate vector $\mathbf{D}(c)$ as

$$757 \quad \mathbf{T}_1 = \frac{1}{\xi_x \xi_x} [1 \ 0 \ 0 \ 0], \quad \mathbf{T}_2 = \frac{1}{\xi_x \xi_z} [0 \ 1 \ 0 \ 0], \quad \mathbf{T}_3 = \frac{1}{\xi_x \xi_z} [0 \ 0 \ 1 \ 0], \quad \mathbf{T}_4 = \frac{1}{\xi_z \xi_z} [0 \ 0 \ 0 \ 1], \quad (A-1)$$

$$758 \quad \mathbf{D}(c) = [\partial_x(c\partial_x) \ \partial_x(c\partial_z) \ \partial_z(c\partial_x) \ \partial_z(c\partial_z)], \quad (A-2)$$

759 where ξ_x and ξ_z are the PML damping function, c represents effective stiffness. Then, the expression of A_c, B_c, C_c, D_c are
 760 written in matrix form:

$$761 \quad \begin{bmatrix} A_c \\ B_c \\ C_c \\ D_c \end{bmatrix} = \begin{bmatrix} \mathbf{D}(c_{11}) & \mathbf{D}(c_{15}) & \mathbf{D}(c_{15}) & \mathbf{D}(c_{55}) \\ \mathbf{D}(c_{15}) & \mathbf{D}(c_{55}) & \mathbf{D}(c_{13}) & \mathbf{D}(c_{35}) \\ \mathbf{D}(c_{15}) & \mathbf{D}(c_{13}) & \mathbf{D}(c_{55}) & \mathbf{D}(c_{35}) \\ \mathbf{D}(c_{55}) & \mathbf{D}(c_{35}) & \mathbf{D}(c_{35}) & \mathbf{D}(c_{33}) \end{bmatrix} \begin{bmatrix} \mathbf{T}_1 \\ \mathbf{T}_2 \\ \mathbf{T}_3 \\ \mathbf{T}_4 \end{bmatrix}. \quad (A-3)$$

762 We formulate A_r, B_r, C_r, D_r in a similar way by defining the coefficient vectors \mathbf{T}'_k ($k = 1, 2, 3, 4$) and $\mathbf{D}'(c)$ as

$$763 \quad \mathbf{T}'_1 = \frac{1}{2\xi_x \xi_x} [1 \ 1 \ 1 \ 1], \quad \mathbf{T}'_2 = \frac{1}{2\xi_x \xi_z} [-1 \ 1 \ -1 \ 1], \quad \mathbf{T}'_3 = \frac{1}{2\xi_x \xi_z} [-1 \ -1 \ 1 \ 1], \quad \mathbf{T}'_4 = \frac{1}{2\xi_z \xi_z} [1 \ -1 \ -1 \ 1], \quad (A-4)$$

$$764 \quad \mathbf{D}'(c) = [\partial_{x'}(c\partial_{x'}) \ \partial_{x'}(c\partial_{z'}) \ \partial_{z'}(c\partial_{x'}) \ \partial_{z'}(c\partial_{z'})], \quad (A-5)$$

765 The expression of A_r, B_r, C_r, D_r are written as

$$766 \quad \begin{bmatrix} A_r \\ B_r \\ C_r \\ D_r \end{bmatrix} = \begin{bmatrix} \mathbf{D}'(c_{11}) & \mathbf{D}'(c_{15}) & \mathbf{D}'(c_{15}) & \mathbf{D}'(c_{55}) \\ \mathbf{D}'(c_{15}) & \mathbf{D}'(c_{55}) & \mathbf{D}'(c_{13}) & \mathbf{D}'(c_{35}) \\ \mathbf{D}'(c_{15}) & \mathbf{D}'(c_{13}) & \mathbf{D}'(c_{55}) & \mathbf{D}'(c_{35}) \\ \mathbf{D}'(c_{55}) & \mathbf{D}'(c_{35}) & \mathbf{D}'(c_{35}) & \mathbf{D}'(c_{33}) \end{bmatrix} \begin{bmatrix} \mathbf{T}'_1 \\ \mathbf{T}'_2 \\ \mathbf{T}'_3 \\ \mathbf{T}'_4 \end{bmatrix}. \quad (A-6)$$

767 Appendix B: Parsimonious staggered-grid stencil

768 The nine coefficients of the CS stencil for the submatrix \mathbf{A}_c of Eq. (36):

769 $A_{c i+1,j} = \frac{c_{11 i+0.5,j}}{\Delta^2 \xi_x i \xi_x i+0.5}, A_{c i-1,j} = \frac{c_{11 i-0.5,j}}{\Delta^2 \xi_x i \xi_x i-0.5}, A_{c i,j+1} = \frac{c_{55 i,j+0.5}}{\Delta^2 \xi_z j \xi_z j+0.5}, A_{c i,j-1} = \frac{c_{55 i,j-0.5}}{\Delta^2 \xi_z j \xi_z j-0.5},$

770 $A_{c i,j} = -\frac{c_{11 i+0.5,j}}{\Delta^2 \xi_x i \xi_x i+0.5} - \frac{c_{11 i-0.5,j}}{\Delta^2 \xi_x i \xi_x i-0.5} - \frac{c_{55 i,j+0.5}}{\Delta^2 \xi_z j \xi_z j+0.5} - \frac{c_{55 i,j-0.5}}{\Delta^2 \xi_z j \xi_z j-0.5}, A_{c i+1,j+1} = \frac{c_{15 i+1,j} + c_{15 i,j+1}}{4\Delta^2 \xi_x i \xi_z j},$

771 $A_{c i+1,j-1} = -\frac{c_{15 i+1,j} + c_{15 i,j-1}}{4\Delta^2 \xi_x i \xi_z j}, A_{c i-1,j+1} = -\frac{c_{15 i-1,j} + c_{15 i,j+1}}{4\Delta^2 \xi_x i \xi_z j}, A_{c i-1,j-1} = \frac{c_{15 i-1,j} + c_{15 i,j-1}}{4\Delta^2 \xi_x i \xi_z j}. \quad (\text{B-1})$

772 The nine coefficients of the RS stencil for the submatrix \mathbf{A}_r of Eq. (36):

773 $A_{r i+1,j} = \frac{c_{11 i+0.5,j-0.5} - c_{55 i+0.5,j-0.5}}{4\Delta^2 \xi_x i \xi_z j-0.5} + \frac{c_{11 i+0.5,j+0.5} - c_{55 i+0.5,j+0.5}}{4\Delta^2 \xi_z j \xi_x i+0.5}, A_{r i-1,j} = \frac{c_{11 i-0.5,j+0.5} - c_{55 i-0.5,j+0.5}}{4\Delta^2 \xi_x i \xi_z j+0.5} + \frac{c_{11 i-0.5,j-0.5} - c_{55 i-0.5,j-0.5}}{4\Delta^2 \xi_z j \xi_x i-0.5},$

774 $A_{r i,j+1} = \frac{c_{55 i-0.5,j+0.5} - c_{11 i-0.5,j+0.5}}{4\Delta^2 \xi_x i \xi_z j+0.5} + \frac{c_{55 i+0.5,j+0.5} - c_{11 i+0.5,j+0.5}}{4\Delta^2 \xi_z j \xi_x i+0.5}, A_{r i,j-1} = \frac{c_{55 i+0.5,j-0.5} - c_{11 i+0.5,j-0.5}}{4\Delta^2 \xi_x i \xi_z j-0.5} + \frac{c_{55 i-0.5,j-0.5} - c_{11 i-0.5,j-0.5}}{4\Delta^2 \xi_z j \xi_x i-0.5},$

775 $A_{r i,j} = -\frac{c_{11 i+0.5,j-0.5} - 2c_{15 i+0.5,j-0.5} + c_{55 i+0.5,j-0.5}}{4\Delta^2 \xi_x i \xi_x i+0.5} - \frac{c_{11 i-0.5,j+0.5} - 2c_{15 i-0.5,j+0.5} + c_{55 i-0.5,j+0.5}}{4\Delta^2 \xi_x i \xi_x i-0.5} \\ - \frac{c_{11 i+0.5,j+0.5} + 2c_{15 i+0.5,j+0.5} + c_{55 i+0.5,j+0.5}}{4\Delta^2 \xi_z j \xi_z j+0.5} - \frac{c_{11 i-0.5,j-0.5} + 2c_{15 i-0.5,j-0.5} + c_{55 i-0.5,j-0.5}}{4\Delta^2 \xi_z j \xi_z j-0.5}$

776 $A_{r i+1,j+1} = \frac{c_{11 i+0.5,j+0.5} + 2c_{15 i+0.5,j+0.5} + c_{55 i+0.5,j+0.5}}{4\Delta^2 \xi_z j \xi_z j+0.5}, A_{r i+1,j-1} = \frac{c_{11 i+0.5,j-0.5} - 2c_{15 i+0.5,j-0.5} + c_{55 i+0.5,j-0.5}}{4\Delta^2 \xi_x i \xi_x i+0.5},$

777 $A_{r i-1,j+1} = \frac{c_{11 i-0.5,j+0.5} - 2c_{15 i-0.5,j+0.5} + c_{55 i-0.5,j+0.5}}{4\Delta^2 \xi_x i \xi_x i-0.5}, A_{r i-1,j-1} = \frac{c_{11 i-0.5,j-0.5} + 2c_{15 i-0.5,j-0.5} + c_{55 i-0.5,j-0.5}}{4\Delta^2 \xi_z j \xi_z j-0.5}. \quad (\text{B-2})$

778 The coefficients of the submatrices $\mathbf{B}_c, \mathbf{C}_c, \mathbf{D}_c$ and $\mathbf{B}_r, \mathbf{C}_r, \mathbf{D}_r$ can be inferred easily from those of submatrix \mathbf{A}_c and \mathbf{A}_r ,
779 respectively.

780 Acknowledgments

781 This research was financially supported by the National Natural Foundation of China (grant nos. 41874143 and 41574130)
782 and the Key Program of Natural Science Foundation of Sichuan Province (No. 23NSFC0139).

783 References

784 Barbosa, N. D., Rubino J. G., Caspary E., and Holliger K.: Extension of the classical linear slipmodel for fluid-saturated
785 fractures: Accounting for fluid pressure diffusion effects, J. Geophys. Res., 122, 1302-1323, doi:10.1002/2016JB013636,
786 2016a.

787 Barbosa, N. D., Rubino J. G., Caspary E., Milani M., and Holliger K.: Fluid pressure diffusion effects on the seismic reflectivity
788 of a single fracture, J. Acoust. Soc. Am., 140, 2554-2570, doi:10.1121/1.4964339, 2016b.

789 Biot, M. A.: Theory of elastic waves in a fluid-saturated porous solid. I. Low frequency range, *J. Acoust. Soc. Am.*, 28, 168-
790 178, doi:10.1121/1.1908239, 1956a.

791 Biot, M. A.: Theory of elastic waves in a fluid-saturated porous solid. II. High frequency range, *J. Acoust. Soc. Am.*, 28, 179-
792 191, doi:10.1121/1.1908241, 1956b.

793 Brajanovski, M., Gurevich, B., and Schoenberg, M.: A model for P-wave attenuation and dispersion in a porous medium
794 permeated by aligned fractures, *Geophys. J. Int.*, 163, 372-384, doi:10.1111/j.1365-246X.2005.02722.x, 2005.

795 Brajanovski, M., Müller T. M., and Gurevich B.: Characteristic frequencies of seismic attenuation due to wave-induced fluid
796 flow in fractured porous media, *Geophys. J. Int.*, 166, 574-578, doi:10.1111/j.1365-246X.2006.03068.x, 2006.

797 Chapman, M.: Frequency dependent anisotropy due to mesoscale fractures in the presence of equant porosity, *Geophys.*
798 *Prospect.*, 51, 369-379, doi:10.1046/j.1365-2478.2003.00384.x, 2003.

799 Coates, R. T. and Schoenberg, M.: Finite-difference modeling of faults and fractures, *Geophysics*, 60, 1514-1526,
800 doi:10.1190/1.1443884, 1995.

801 Cui, X. Q., Lines, L. R., and Krebes, E. S.: Seismic modelling for geological fractures, *Geophys. Prospect.*, 2018, 157-168,
802 doi:10.1111/1365-2478.12536, 2018.

803 Dutta, N. C. and Odé, H.: Attenuation and dispersion of compressional waves in fluid-filled porous rocks with partial gas
804 saturation (White Model)-Part I: Biot theory, *Geophysics*, 44, 1777-1788, doi:10.1190/1.1440938, 1979a.

805 Dutta, N. C. and Odé, H.: Attenuation and dispersion of compressional waves in fluid-filled porous rocks with partial gas
806 saturation (White Model)-Part II: Results, *Geophysics*, 44, 1806-1812, doi:10.1190/1.1440939, 1979b.

807 Gale, J. F. W., Laubach S. E., Olson J. E., Eichhubl P., and Fall A.: Natural fractures in shale: A review and new observations:
808 AAPG Bulletin, 98, 2165-2216, doi:10.1306/08121413151, 2014.

809 Galvin, R. J. and Gurevich, B.: Frequency-dependent anisotropy of porous rocks with aligned fractures, *Geophys. Prospect.*,
810 63, 141-150, doi:10.1071/ASEG2003ab016, 2015.

811 Gassmann, F.: Elastic waves through a packing of spheres, *Geophysics*, 16, 673-685, doi:10.1190/1.1437718, 1951.

812 Gavagnin, C., Sanavia, L., and Lorenzis, L. D.: Stabilized mixed formulation for phase-field computation of deviatoric fracture
813 in elastic and poroelastic materials, *Comput Mech*, 65, 1447-1465, doi:10.1007/s00466-020-01829-x, 2020.

814 Gelinsky, S. and Shapiro, S. A.: Dynamic-equivalent medium approach for thinly layered saturated sediments, *Geophys. J. Int.*,
815 128, F1-F4, doi:10.1111/j.1365-246X.1997.tb04086.x, 1997.

816 Guo J. X., Rubino J. G., Barbosa, N. D., Glubokovskikh, S. G., and Gurevich, B.: Seismic dispersion and attenuation in
817 saturated porous rocks with aligned fractures of finite thickness: Theory and numerical simulations—Part I: P-wave
818 perpendicular to the fracture plane, *Geophysics*, 83, 49-62, doi:10.1190/geo2017-0065.1, 2017a.

819 Guo J. X., Rubino J. G., Barbosa, N. D., Glubokovskikh, S. G., and Gurevich, B.: Seismic dispersion and attenuation in
820 saturated porous rocks with aligned fractures of finite thickness: Theory and numerical simulations—Part II: Frequency-

821 dependent anisotropy, *Geophysics*, 83, 63-71, doi:10.1190/geo2017-0066.1, 2017b.

822 Gurevich, B., Zyrianov, V. B., and Lopatnikov, S. L.: Seismic attenuation in finely layered porous rocks: Effects of fluid flow
823 and scattering, *Geophysics*, 62(1), 319-324, doi:10.1190/1.1444133, 1997.

824 Gurevich, B.: Elastic properties of saturated porous rocks with aligned fractures, *J. Geophys. Res.*, 54, 203-218,
825 doi:10.1016/j.jappgeo.2002.11.002, 2003.

826 Hustedt, B., Operto S., and Virieux J.: Mixed-grid and staggered-grid finite difference methods for frequency domain acoustic
827 wave modelling, *Geophys J Int*, 157, 1269-1296, doi:10.1111/j.1365-246X.2004.02289.x, 2004.

828 Johnson, D. L.: Theory of frequency dependent acoustics in patchy-saturated porous media, *J. Acoust. Soc. Am.*, 110(2), 682-
829 694, doi:10.1121/1.1381021, 2001.

830 Jo, C.H., Shin, C.S., and Suh, J.H.: An optimal 9-point, finite-difference, frequency-space, 2-D scalar wave extrapolator,
831 *Geophysics*, 61, 529-537, doi:10.1190/1.1443979, 1996.

832 Khokhlov, N., Favorskaya, A., Stetsyuk, V., Mitskovets, I.: Grid-characteristic method using Chimera meshes for simulation
833 of elastic waves scattering on geological fractured zones, *J. Comput. Phys.*, 446, 110637, doi:10.1016/j.jcp.2021.110637,
834 2021.

835 Krzikalla, F. and Müller T. M.: Anisotropic P-SV-wave dispersion and attenuation due to inter-layer flow in thinly layered
836 porous rocks, *Geophysics*, 76, WA135-WA145, doi:10.1190/1.3555077, 2011.

837 Kudarova, A. M., Karel, V. D., and Guy D.: An effective anisotropic poroelastic model for elastic wave propagation in finely
838 layered media, *Geophysics*, 81, 175-188, doi:10.1190/geo2015-0362.1, 2016.

839 Liu E. R., Hudson J. A., and Pointer T.: Equivalent medium representation of fractured rock, *J. Geophys. Res.*, 105, 2981-3000,
840 doi:10.1029/1999JB900306, 2000.

841 Liu, X., Greenhalgh, S., Zhou, B., and Greenhalgh, M.: Frequency-domain seismic wave modelling in heterogeneous porous
842 media using the mixed-grid finite-difference method, *Geophys J Int.*, 216, 34-54, doi:10.1093/gji/ggy410, 2018.

843 Müller, T. M., Stewart J. T., and Wenzlau, F.: Velocity-saturation relation for partially saturated rocks with fractal pore fluid
844 distribution, *Geophys. Res. Lett.*, 35, L09306, doi:10.1029/2007GL033074, 2008.

845 Nakagawa, S. and Schoenberg M. A.: Poroelastic modeling of seismic boundary conditions across a fracture, *J. Acoust. Soc.*
846 *Am.*, 122, 831-847, doi:10.1121/1.2747206, 2007.

847 Norris, A. N.: Low-frequency dispersion and attenuation in partially saturated rocks, *J. Acoust. Soc. Am.*, 94, 359-370,
848 doi:10.1121/1.407101, 1993.

849 Oelke, A., Alexandrov, D., Abakumov, I., Glubokovskikh, S., Shigapov, R., Krüger, O. S., Kashtan, B., Troyan, V., and Shapiro,
850 S. A.: Seismic reflectivity of hydraulic fractures approximated by thin fluid layers, *Geophysics*, 78, 79-87,
851 doi:10.1190/geo2012-0269.1, 2013

852 Operto, S., Virieux, J., Ribodetti, A., and Anderson J. E.: Finite-difference frequency-domain modeling of viscoacoustic wave

853 propagation in 2D tilted transversely isotropic (TTI) media, *Geophysics*, 74, 75-95, doi:10.1190/1.3157243, 2009.

854 Rubino, J. G., Müller T. M., Guerracino L., Milani M., and Holliger K.: Seismoacoustic signatures of fracture connectivity, *J.*
855 *Geophys. Res. Solid Earth.*, 119, 2252-2271, doi:10.1002/2013JB010567, 2014.

856 Rubino, J. G., Castromán G. A., Müller T. M., Monachesi L. B., Zyserman F. I., and Holliger K.: Including poroelastic effects
857 in the linear slip theory, *Geophysics*, 80, A51-A56, doi:10.1190/geo2014-0409.1, 2015.

858 Sayers, C. M. and Kachanov M.: Microcrack-induced elastic wave anisotropy of brittle rocks, *J. Geophys. Res.*, 100, 4149-
859 4156, doi:10.1029/94JB03134, 1995.

860 Schoenberg, M. A.: Elastic wave behavior across linear slip interfaces, *J. Acoust. Soc. Am.*, 68, 1516-1521,
861 doi:10.1121/1.385077, 1980.

862 White, J. E., Mikhahaylova, N. G., and Lyakhovitsky, F. M.: Low-frequency seismic waves in fluid-saturated layered rocks,
863 *Izv., Acad. Sci., USSR, Phys. Solid Earth.*, 11, 654-659, doi:10.1121/1.1995164, 1975.

864 Zhang, J. F.: Elastic wave modeling in fractured media with an explicit approach, *Geophysics*, 70, 75-85,
865 doi:10.1190/1.2073886, 2005.